



HAL
open science

Direct temporal cascade of temperature variance in eddy-permitting simulations of multidecadal variability

Antoine Hochet, Thierry Huck, Olivier Arzel, Florian Sévellec, Alain Colin de Verdière, Matthew Mazloff, Bruce Cornuelle

► **To cite this version:**

Antoine Hochet, Thierry Huck, Olivier Arzel, Florian Sévellec, Alain Colin de Verdière, et al.. Direct temporal cascade of temperature variance in eddy-permitting simulations of multidecadal variability. *Journal of Climate*, 2020, 33 (21), pp.9409-9425. 10.1175/JCLI-D-19-0921.1 . hal-02953817

HAL Id: hal-02953817

<https://hal.science/hal-02953817>

Submitted on 30 Sep 2020

HAL is a multi-disciplinary open access archive for the deposit and dissemination of scientific research documents, whether they are published or not. The documents may come from teaching and research institutions in France or abroad, or from public or private research centers.

L'archive ouverte pluridisciplinaire **HAL**, est destinée au dépôt et à la diffusion de documents scientifiques de niveau recherche, publiés ou non, émanant des établissements d'enseignement et de recherche français ou étrangers, des laboratoires publics ou privés.



1 **Direct temporal cascade of temperature variance in eddy-permitting**

2 **simulations of multidecadal variability**

3 Antoine Hochet* ,Thierry Huck, Olivier Arzel, Florian Sévellec and Alain Colin de Verdière

4 *Univ Brest, CNRS, Ifremer, IRD, Laboratoire d'Océanographie Physique et Spatiale (LOPS,*

5 *UMR 6523), IUEM, Brest, France*

6 Matthew Mazloff and Bruce Cornuelle

7 *Scripps institution of Oceanography, La Jolla, California, USA.*

8 *Corresponding author address: Antoine Hochet, Laboratoire d'Océanographie Physique et Spa-
9 tiale (LOPS, UMR 6523 Univ Brest, CNRS, Ifremer, IRD), Brest, France

10 E-mail: antoine.hochet@univ-brest.fr

Generated using v4.3.2 of the AMS L^AT_EX template

1

Early Online Release: This preliminary version has been accepted for publication in *Journal of Climate*, may be fully cited, and has been assigned DOI 10.1175/JCLI-D-19-0921.1. The final typeset copyedited article will replace the EOR at the above DOI when it is published.

© 2020 American Meteorological Society

ABSTRACT

11 The North Atlantic is characterized by basin-scale multidecadal fluctuations
12 of the sea surface temperature with periods ranging from 20 to 70 years. One
13 candidate for such a variability is a large-scale baroclinic instability of the
14 temperature gradients across the Atlantic associated with the North Atlantic
15 Current. Because of the long time scales involved, most of the studies de-
16 voted to this problem are based on low resolution numerical models leaving
17 aside the effect of explicit meso-scale eddies. How high-frequency motions
18 associated with the meso-scale eddy field affect the basin-scale low-frequency
19 variability is the central question of this study.

20 This issue is addressed using an idealized configuration of an Ocean General
21 Circulation Model at eddy-permitting resolution (20 km). A new diagnostic
22 allowing the calculation of nonlinear fluxes of temperature variance in fre-
23 quency space is presented. Using this diagnostic, we show that the primary
24 effect of meso-scale eddies is to damp low frequency temperature variance
25 and to transfer it to high frequencies.

26 **1. Introduction**

27 The existence of basin-scale multidecadal fluctuations of the North Atlantic Sea Surface Tem-
28 perature (SST) is long established (Bjerknes 1964; Kushnir 1994). It consists of a horseshoe
29 pattern of SST anomaly extending from the subpolar gyre to the tropics and a weaker anomaly of
30 opposite sign south of the equator (Kushnir 1994; Deser et al. 2010; Zhang et al. 2019). Proxy
31 records across the North Atlantic have demonstrated the ubiquitous nature of this Low Frequency
32 (LF) variability (Knudsen et al. 2011) over the past 8000 years. This multidecadal variability has
33 periods in the range 20-70 years (Folland et al. 1984, 1986; Chylek et al. 2011) and is mostly re-
34 ferred to as the Atlantic Multidecadal Variability (AMV) to emphasize the fact that the variability
35 is not an harmonic oscillation at a single frequency but consists of a broader band of low-frequency
36 signals (Zhang 2017).

37 An AMV index can be defined as a ten-year running mean of linearly detrended SST anomalies
38 averaged north of the equator in the Atlantic (Enfield et al. 2001). Positive phases of this index oc-
39 curred during the middle of the twentieth century and since 1995, negative phases occurred during
40 the early 20th century and during the 1964-1995 period. The large-scale LF variability has sig-
41 nificant impacts on the Sahel/Indian summer monsoon rainfall, Atlantic hurricanes frequency and
42 summer climate over western Europe and North America. See Zhang et al. (2019) and references
43 therein for an extensive list of possible impacts of AMV on climate.

44 Three main mechanisms have been proposed to explain the observed low frequency SST varia-
45 tion. Because of the lack of data on such long time scales, no clear consensus has emerged. The
46 first (controversial) one is linked with radiative forcings from anthropogenic aerosols and green-
47 house gases (e.g. Watanabe and Tatebe 2019, and references therein). The second one is related
48 to the integration of the atmospheric white noise by the ocean giving rise to a reddened spectrum

49 (Hasselmann 1976; Frankignoul and Hasselmann 1977). The third mechanism has dynamical ori-
50 gins and is related to intrinsically unstable multidecadal ocean modes. The relative contributions
51 of these paradigms to the observed low-frequency variability of the North Atlantic climate contin-
52 ues to be fiercely debated (Clement et al. 2015; Zhang et al. 2016; O’Reilly et al. 2016; Gastineau
53 et al. 2018; Zhang et al. 2019). The work presented in this paper focuses on the physics of intrinsic
54 ocean modes.

55 Using a coupled general circulation model (CGCM), Delworth et al. (1993) were able to re-
56 produce the pattern and time scale of the variability, and concluded that the AMV is intimately
57 related to AMOC changes. Since then, the linkage between multidecadal AMOC variability and
58 AMV has been found in many CGCMs (e.g. Delworth and Mann 2000; Danabasoglu et al. 2012;
59 Keenlyside et al. 2016; Drews and Greatbatch 2017; Kim et al. 2018). Ba et al. (2014) performed
60 a multi-model analysis of the AMV and found that in eight of the ten models they considered,
61 mid-latitude SST variations are correlated with AMOC fluctuations. Numerous other studies em-
62 ploying CGCMs (Delworth and Greatbatch 2000; Cheng et al. 2004; Dong and Sutton 2005) con-
63 cluded that the variability is due to a damped internal mode of the ocean, forced by atmosphere
64 stochastic forcing. Wills et al. (2019) suggested that the atmospheric response to extra-tropical
65 SST anomalies is essential to explain the AMV amplitude but that it is the ocean circulation that
66 sustains SST anomalies on longtime scales. Observations and high resolution CGCM support the
67 idea that the recent cooling trend in the subpolar North Atlantic upper ocean temperature since
68 2005 is closely linked to the observed decline in the AMOC (Robson et al. 2016).

69 A complementary approach to the one employing statistical analyses of CGCM outputs consists
70 of isolating the “simplest” configuration where interdecadal variability exists and decreasing step
71 by step the degree of idealisation (Greatbatch and Zhang 1995; Chen and Ghil 1996; Zu et al.
72 2013; Colin de Verdière and Huck 1999; Huck et al. 1999, 2001; Te Raa and Dijkstra 2002; Di-

73 jkstra and Ghil 2005; Arzel et al. 2007; Sévellec and Huck 2015; Arzel et al. 2007; Huck et al.
74 2015; Jamet et al. 2016; Arzel et al. 2018). The mode's existence was first shown in a rectan-
75 gular flat-bottomed single-hemispheric basin, with prescribed surface heat fluxes and Planetary
76 Geostrophic dynamics (Greatbatch and Zhang 1995; Colin de Verdière and Huck 1999). In this
77 configuration, a large scale baroclinic instability continuously feeds a large scale mode that gives
78 rise to SST variability which is associated geostrophically with the Meridional Overturning Cir-
79 culation (Colin de Verdière and Huck 1999; Te Raa and Dijkstra 2002). The period of the mode
80 is explained by the basin transit time of temperature anomalies set by the combination of Rossby
81 waves and geostrophic self-advection. The same mode of variability was later demonstrated to
82 exist in a realistic configuration of the North Atlantic (Sévellec and Fedorov 2013). Arzel et al.
83 (2018) further showed that the internal ocean mode produces maximum SST variance in the west-
84 ern part of the subpolar gyre, in agreement with the observed signature of the AMO in the North
85 Atlantic.

86 Sensitivity studies carried out at low resolution based on either idealized or realistic oceanic con-
87 figurations have demonstrated the critical influence of the horizontal and eddy-induced turbulent
88 diffusivities on the properties of the internal ocean mode (e.g. Huck et al. 2001; Arzel et al. 2018).
89 More specifically, the variability disappears for diffusivity values that are typically in the range of
90 observational estimates ($500 - 1000 \text{ m}^2 \text{ s}^{-1}$) casting therefore some doubts on the relevance of this
91 self-sustained internal mode for the observed variability. The same conclusions are found for the
92 influence of the isopycnal diffusivity within the Gent and McWilliams (1990) parameterization in
93 a realistic configuration (Arzel et al. 2018). Moreover, (LaCasce and Pedlosky 2004) have shown
94 that large-scale anomalies associated with Rossby waves are prone to meso-scale baroclinic in-
95 stability; they further suggested that the presence of Rossby waves in the mid to high latitudes is
96 unlikely because at these latitudes, Rossby wave periods are slow compared to the destabilization

97 time scale. In contrast, the study of Huck et al. (2015) suggested that the large-scale mode is robust
98 to meso-scale turbulence. Using a series of experiments from coarse up to eddy-resolving (10 km)
99 resolutions, these authors showed that the spatial structure of the mode is modified, in agreement
100 with the changes in the mean state as the resolution is refined, however, the main period and phys-
101 ical mechanism of the mode remains robust. An explanation for this apparent contradiction could
102 be that instead of being a freely evolving mode as in LaCasce and Pedlosky (2004), the large-scale
103 mode is continuously extracting energy from the mean flow through a large-scale baroclinic insta-
104 bility, allowing it to overcome the eddy induced dissipation.

105 Even if some studies suggest that the mode is robust to meso-scale turbulence, the interaction be-
106 tween the low frequencies and the high frequencies associated with turbulence remains an open
107 question. Indeed Huck et al. (2015) speculated that because the range of vertical diffusivity coef-
108 ficient (K_v , hereafter) allowing the existence of the low-frequency mode is larger at eddy-resolving
109 than at low resolution, the eddy field may in fact act as a stochastic excitation of the low-frequency
110 mode. This idea is reminiscent of the studies of Frankcombe et al. (2009); Sévellec et al. (2009);
111 Arzel and Huck (2020) who suggested that the SST multidecadal temperature variability could
112 be explained by a damped oceanic mode forced by atmospheric noise. Juricke et al. (2017) sug-
113 gested that the low frequency variability at coarse resolution can be better simulated by enhanced
114 subgrid-scale variability, where the latter is included by applying stochastic perturbations to the
115 GM scheme. Additionally, a recent series of studies (Arbic et al. 2012, 2014; Sérazin et al. 2015;
116 O’Rourke et al. 2018; Sérazin et al. 2018) further suggests that meso-scale eddies undergo what
117 has been called a “temporal inverse cascade of kinetic energy”. This cascade is reflected in a
118 transfer of kinetic energy from the high frequency meso-scale eddy field to lower frequencies and
119 seems to support the idea of a possible forcing of the low frequency mode by meso-scale eddies.
120 However there seems to be a contradiction between the idea that diffusion, which parameterizes

121 the effect of eddies, is a sink of temperature variance and that eddy turbulence might also be a
122 source term for the low frequency mode.

123 In this work we seek to further investigate the effect of high-frequency motions associated with
124 the meso-scale eddy field on the basin-scale low-frequency motions associated with the internal
125 ocean mode. More specifically, we aim to determine the direction and intensity of these nonlinear
126 temperature variance fluxes in frequency space. We choose here to focus on temperature variance
127 rather than on Available Potential Energy for several reasons. 1) It is a variable that is directly
128 measurable (unlike Available Potential Energy); 2) The effect of AMV is predominantly observed
129 in SST; 3) The temperature variance budget has been extensively used in studies on intrinsic in-
130 terdecadal variability of the ocean (e.g. Colin de Verdière and Huck (1999); Arzel et al. (2006,
131 2007); Buckley et al. (2012); Jamet et al. (2016); Arzel et al. (2018); Gastineau et al. (2018)) and
132 has proved to be a powerful tool to understand its underlying mechanism. Here a new method is
133 developed to compute these fluxes and applied to the simplest setup where both the large-scale
134 LF mode and meso-scale eddies are known to exist: a flat-bottom, single hemispheric, rectangu-
135 lar basin forced only by constant heat fluxes at the surface with eddy-permitting resolution. The
136 limited extent of the grid due to the single hemispheric basin allows for the simulation of both low
137 frequency (20 to 50 years) and high frequency variability.

138 The article is organised as follows: in section 2, the numerical setup, the mean state, and the
139 low and high-frequency variability are described. In section 3, we present a new diagnostic that
140 is used to study the temperature variance fluxes in frequency space. In section 4, we derive an
141 equation for the low-frequency temperature variance, and show in physical space the influence of
142 meso-scale eddy variability on the LF variance. In the last section we conclude and discuss our
143 results.

2. Model description, mean flow and variability

a. Model description

We use the MITgcm (Marshall et al. 1997) in a rectangular flat bottom basin with a Cartesian geometry on a β -plane centered at 40°N . The zonal and meridional extents are respectively $L_x = 5000\text{ km}$ ($\approx 47^\circ$ at 20°N) and $L_y = 4500\text{ km}$ ($\approx 40^\circ$), and the Southern boundary is located 2000 km north of the equator. An eddy-permitting horizontal resolution of 20 km is used in both directions. Huck et al. (2015) used higher resolution, up to 10 km , but despite a stronger intensity of the meso-scale eddy field at the highest resolution, no qualitative changes in the characteristics of the multidecadal variability were found between the 10 and 20 km runs. The depth is $H = 4500\text{ m}$ and there are 40 levels in the vertical with grid spacing increasing from 10 m at the surface to 400 m at the bottom.

The ocean is forced by a steady heat flux at the surface. This flux is zonally uniform and decreases linearly with latitude from 50 W m^{-2} at $y = 0\text{ km}$ to -50 W m^{-2} at $y = 4500\text{ km}$, similar to Huck et al. (2015). Since our focus is on the physics of the low-frequency variability forced by prescribed surface heat fluxes, wind-stress forcing is set to zero in our experiments. The effect of the wind-stress forcing has been studied extensively in Quasi-Geostrophic models and was shown to produce sub-decadal gyre variability (e.g. Berloff and McWilliams 1999; Simonnet and Dijkstra 2002; Berloff et al. 2007). How wind-stress forcing affects the results of the present study remains to be addressed. A linear equation of state is used with temperature as the only active tracer and the thermal expansion coefficient is assumed uniform with a value of $\alpha = 2 \times 10^{-4}\text{ K}^{-1}$. Horizontal biharmonic eddy diffusivity and viscosity are used with the same uniform value of $10^{11}\text{ m}^4\text{ s}^{-1}$. The vertical viscosity is $\nu_v = 10^{-3}\text{ m}^2\text{ s}^{-1}$. No Gent-McWilliams parametrization (Gent and McWilliams 1990) is used. Static instability is removed by enhanced mixing of the

167 water column (to $100 \text{ m}^2 \text{ s}^{-1}$). In this single hemispheric basin, the MOC strength (defined below)
 168 is strongly dependent on the value of the vertical diffusivity K_v , in agreement with the classical
 169 geostrophic scaling in the vertical advective-diffusive balance showing a $K_v^{1/2}$ law for the strength
 170 of the MOC under prescribed surface fluxes (Huang and Chou 1994; Huck et al. 1999). Hence,
 171 we choose to use $K_v = 2 \times 10^{-4} \text{ m}^2 \text{ s}^{-1}$ to obtain a MOC strength close to 10 Sv.

172 *b. Time mean circulation and low-frequency variability*

173 Under this configuration, LF variability of the temperature field spontaneously develops. A de-
 174 tailed description of the variability developing in very similar geometries can be found for instance
 175 in Huck et al. (1999); Huck and Vallis (2001); Huck et al. (2015). Here we will only give a short
 176 description of its main characteristics. The LF variability of the three dimensional temperature
 177 field is well described by the first Complex Empirical Orthogonal Function (CEOF hereafter) that
 178 contains 60% of the temperature variance. The CEOF are calculated using 20 days average out-
 179 puts on a 300 years long simulation. Similar to the widely used empirical orthogonal function,
 180 CEOF are the eigenvectors of the complex covariance matrix of a complex temperature anomaly
 181 which is calculated using the Hilbert transform of the detrended temperature anomaly (Von Storch
 182 and Zwiers 2001). CEOF are more suitable than EOF to describe propagating features: the large-
 183 scale mode is indeed contained in a single CEOF while it would require two EOFs to describe the
 184 same mode. The temperature anomaly associated to a CEOF can then be reconstructed using the
 185 following formula:

$$\theta_{\text{CEOF}}(x, y, z, t) = \text{PC}_{re}(t)\text{CEOF}_{re}(x, y, z) + \text{PC}_{im}(t)\text{CEOF}_{im}(x, y, z) \quad (1)$$

186 where *re* and *im* stand for respectively the real and imaginary part and PC is the principal compo-
 187 nent of the corresponding CEOF. Fig. 1 shows that the low-frequency variability takes the form of

188 a large-scale temperature anomaly propagating northward, located mainly in the northwestern half
 189 and in the upper 500 m of the basin with SST anomaly larger than 3 K at some locations. Contours
 190 of the time mean temperature are also shown on the same figure; mean temperature decreases
 191 northward with isotherms outcropping in the northern half of the basin. In the absence of surface
 192 wind-stress forcing, box-ocean models show a single thermally-driven anticyclonic gyre with a
 193 western boundary current that remains attached to the coast from tropical to subpolar latitudes.
 194 The implied poleward heat transport along the western boundary makes the western part of the
 195 subpolar area (typically North of 50 N) always warmer than the eastern part, which is opposed to
 196 what is seen in observations at subpolar latitudes. This difference in the SST climatology does
 197 not have any consequences for either the energy source (i.e. large-scale baroclinic instability) or
 198 the main features of the variability. All these aspects are preserved when using a more realistic
 199 geometry (Sévellec and Fedorov 2013; Arzel et al. 2018; Arzel and Huck 2020).

200 The bottom panel of Figure 1 shows the real and imaginary part of the PC and the time series of
 201 the MOC strength. The MOC strength is defined as the vertical and meridional maximum of the
 202 time mean overturning streamfunction which is:

$$\Psi(y, z, t) = \int_z^0 \int_{x=0}^L v dx dy, \quad (2)$$

203 and the MOC strength is then $\Psi(y_{max}, z_{max}, t)$ with $y_{max} = 3500\text{km}$ and $z_{max} = -500\text{m}$ in this
 204 setup. Following the time evolution of the PC (bottom panel of Fig. 1), the oscillation consists of
 205 four steps separated by one quarter of a cycle: $re \rightarrow im \rightarrow -re \rightarrow -im \rightarrow re$ where re and im are
 206 respectively the real and imaginary part of the CEOF. The minimum MOC strength shown on the
 207 bottom panel of Fig. 1 is correlated with positive anomaly of SST close to the Northern bound-
 208 ary (the first CEOF real part times -1 on the left panel of figure 1). Maximum values of MOC
 209 strength are correlated with negative temperature anomaly being close to the Northern boundary

210 (the first CEOF real part on the left panel of figure 1). The phase of the oscillation represented by
211 the CEOF is chosen so that the correlation between the CEOF PC real part and the MOC strength
212 is maximum. The real part of the PC follows closely the MOC strength time variation giving us
213 confidence that the leading CEOF adequately represents the low frequency variability of our setup.
214 To estimate the period of this low-frequency mode, we calculate the power spectrum of tempera-
215 ture at each grid point and average them. For this calculation we use a 500 year long simulation
216 made of 1 year time average outputs. The temperature spectrum plotted in Figure 2 has a distinct
217 peak at a period of ~ 42 years which is in the range of that found in previous studies. A secondary
218 peak of smaller intensity is found at a period of ~ 21 years and is attributed to the second harmonic
219 of the leading CEOF. In agreement with the comparison of the PC real part and MOC strength on
220 the bottom of figure 1, the MOC strength frequency spectrum also shows a peak at a period of
221 ~ 42 years (fig. 2).

222 *c. High-frequency variability*

223 In the absence of wind forcing, Kinetic Energy (KE) can only be forced through Available
224 Potential Energy (APE) to KE conversion. This unique source of KE creates nonetheless a strong
225 eddy field that, as will be shown below, accounts for more than 50% of the total sink of the low-
226 frequency mode temperature variance. The temperature spectrum calculated with 3-day average
227 outputs on a 50-year simulation is shown in Fig. 2. The spectrum follows two different slopes
228 depending on the frequency: a slight slope for frequencies smaller than $2\pi/3$ months⁻¹ and a
229 steep slope for frequencies larger than $2\pi/3$ months⁻¹. The standard deviation of the Sea Surface
230 Height (SSH) (which is a quantity that is easily observable by satellite altimetry, and can be used
231 to assess eddy activity) with a 2 year running average removed and calculated on the same run,
232 is plotted on the left panel of figure 3. The largest values (around 0.16m) are found close to the

233 Western boundary and in the Northern half of the basin. These values are in the range of observed
 234 values of SSH standard deviation as observed by TOPEX/POSEIDON (Stammer 1997) suggesting
 235 that the level of eddy activity in our simulation is realistic. A snapshot of the ratio of the surface
 236 relative vorticity ($\zeta = \partial_x v - \partial_y u$) normalized by the Coriolis parameter f (Fig. 3, right panel)
 237 reveals the presence of zonally organised eddy features that can also be seen as zonal jets in the
 238 time averaged zonal velocity (Fig. 4). It is interesting to note that the values of this ratio remain
 239 much smaller than 1, so that the geostrophic assumption holds even for the meso-scale turbulence.

240 3. Transfer of temperature variance in frequency space

241 In this section we derive the budget for the transfer of temperature variance in frequency space.
 242 We then study the different temperature fluxes of our setup and show in particular that there is a
 243 nonlinear flux of temperature variance toward higher frequencies.

244 a. Temperature variance fluxes in frequency: definition

245 Given our setup, the temperature θ obeys the following equation:

$$\frac{\partial \theta}{\partial t} + \mathbf{u} \cdot \nabla \theta = D + G \quad (3)$$

246 where \mathbf{u} is the 3D velocity (u, v, w) , D represents the parameterised diffusion and the convection
 247 and G is the surface heat flux. To obtain an equation for the temperature variability, we decompose
 248 all variables into time mean plus anomaly: $X = \bar{X} + X'$ with X being θ, \mathbf{u}, D , or G . $\bar{(\cdot)}$ is the time
 249 mean over the 200 years of the simulation, $(\cdot)'$ is the anomaly with $\bar{X}' = 0$, by construction. Note
 250 that G is time independent and thus equal to its time mean. The time mean of Eq. (3) is:

$$\bar{\mathbf{u}} \cdot \nabla \bar{\theta} + \overline{\mathbf{u}' \cdot \nabla \theta'} = \bar{D} + G, \quad (4)$$

251 The time evolution equation for θ' is obtained by subtracting Eq. (4) from Eq. (3):

$$\frac{\partial \theta'}{\partial t} = -\bar{\mathbf{u}} \cdot \nabla \theta' - \mathbf{u}' \cdot \nabla \bar{\theta} - \mathbf{u}' \cdot \nabla \theta' + \overline{\mathbf{u}' \cdot \nabla \theta'} + D'. \quad (5)$$

252 Transfers in the frequency or in the space domain are usually calculated for KE or APE (see for
 253 instance Arbic et al. 2014, and references therein). The usual way of calculating these QG KE
 254 or APE transfers is to Fourier transform the vorticity equation multiplied by the conjugate of the
 255 Fourier transform of the stream function (more frequently in space but it can also be done in
 256 time). Here we follow this idea but apply it to the temperature and in the frequency domain. The
 257 temperature anomaly θ' is detrended in time and multiplied by a Tukey window, with a value of
 258 0.2 for the ratio of taper to constant sections as in Arbic et al. (2014) in order to obtain a periodic
 259 field in time. Temperature spectral transfers are calculated by multiplying the discrete Fourier
 260 Transform in time of each component of Eq. (5) by the conjugate of the Fourier transform of θ at
 261 every grid point. The result is integrated over the domain to give, in a statistical steady state:

$$0 = \text{Tr}_{\text{mean}}(\omega) + \text{Tr}_{\text{turb}}(\omega) + \text{Tr}_{\text{diss}}(\omega) \quad (6)$$

262 with ω the frequency. The expression for $\text{Tr}_{\text{mean}}(\omega)$ is:

$$\text{Tr}_{\text{mean}}(\omega) = - \int_V \Re \left(\widehat{\theta'}^*(\omega) \left(\widehat{\bar{\mathbf{u}} \cdot \nabla \theta'}(\omega) + \widehat{\mathbf{u}' \cdot \nabla \bar{\theta}}(\omega) \right) \right) dV, \quad (7)$$

263 where \Re is the real part, ω the frequency and V the volume. The spectral transfers identify
 264 temperature variance sources (when positive) or sinks (when negative) in frequency space. Note
 265 that $\bar{\mathbf{u}} \cdot \nabla \theta'$ and $\mathbf{u}' \cdot \nabla \bar{\theta}$ are calculated offline from the values of \mathbf{u} and θ . $\text{Tr}_{\text{mean}}(\omega)$ is interpreted
 266 as the transfer of temperature variance linked with mean flow anomaly interaction. We will show
 267 below that this transfer is a source of temperature variance at every frequency. The formula for
 268 term $\text{Tr}_{\text{turb}}(\omega)$ is:

$$\text{Tr}_{\text{turb}}(\omega) = - \int_V \Re \left(\widehat{\theta'}^*(\omega) \left(\widehat{\mathbf{u}' \cdot \nabla \theta'}(\omega) \right) \right) dV, \quad (8)$$

269 and is interpreted as the transfer of temperature variance by turbulent processes. We will show
 270 that these turbulent transfers are either a source or a sink of temperature variance depending on
 271 the frequency. The last term $\text{Tr}_{\text{diss}}(\omega)$ is:

$$\text{Tr}_{\text{diss}}(\omega) = \int_V \Re \left(\widehat{\theta}'^*(\omega) \widehat{D}'(\omega) \right) dV \quad (9)$$

272 and is the diffusive transfer of temperature variance computed from the actual dissipation output
 273 of the model, a term which will be shown to be negative for every frequency. The term involving
 274 $\overline{\mathbf{u}' \cdot \nabla \theta'}$ disappears when multiplied by $\widehat{\theta}'^*$ because its Fourier transform is nonzero only for $\omega = 0$
 275 and by definition of θ' , $\widehat{\theta}'(\omega = 0) = 0$, so that $\widehat{\theta}'^* \widehat{\overline{\mathbf{u}' \cdot \nabla \theta'}} = 0$.

276 Following other studies (e.g. Scott and Arbic (2007)) we will define and use below spectral fluxes
 277 instead of spectral transfers for the three following reasons: 1) fluxes are much less noisy than the
 278 transfers, 2) as will become clear below, turbulent transfers are zero when integrated over all fre-
 279 quencies and using fluxes makes this fact directly apparent, 3) our interest is on what happens for
 280 a range of frequencies (we will define two ranges below: high-frequencies and low-frequencies)
 281 rather than at a local frequency. The drawback of using spectral fluxes rather than transfers is that
 282 the sign of the transfer needs to be deduced from the sign of the slope of the fluxes which is less
 283 direct than looking directly at the sign of the transfers.

284 We define the spectral fluxes Π of the spectral transfers Tr as:

$$\Pi(\omega) = \int_{\omega}^{\omega_{\max}} \text{Tr}(\omega') d\omega, \quad (10)$$

285 $\Pi_{\text{mean}}(\omega)$, $\Pi_{\text{turb}}(\omega)$ and $\Pi_{\text{diss}}(\omega)$ are respectively the input of temperature variance from the
 286 mean flow, the turbulent terms, and the diffusivity in the frequency domain defined by all ω' with
 287 $\omega' > \omega$. Thus a positive (negative) $\Pi(\omega')$ corresponds to a positive (negative) total input of variance
 288 between ω and ω_{\max} . The total transfer between ω_{\min} and ω is simply: $\Pi(\omega_{\min}) - \Pi(\omega)$. If
 289 $\Pi(\omega_{\min}) - \Pi(\omega)$ is positive (negative) the total transfer between ω_{\min} and ω is positive (negative).

290 Obtaining the transfers from the flux is straightforward:

$$\frac{d\Pi}{d\omega}(\omega) = -Tr(\omega) \quad (11)$$

291 The slope of the Π curve is thus equal to minus the transfer. From Eq. (6) and the flux formula
292 (10) we deduce that :

$$\Pi_{\text{mean}}(\omega) + \Pi_{\text{turb}}(\omega) + \Pi_{\text{diss}}(\omega) = 0, \quad (12)$$

293 i.e. the sum of all fluxes is zero for every frequency.

294

295 *b. Properties of temperature variance fluxes*

296 In this subsection we explain some properties of the temperature variance flux budget (i.e. eq.
297 (12)) that will be useful to interpret results in the next subsection.

298 It is straightforward to show that the effect of the turbulent terms integrated over the volume is
299 zero at each time step. Multiplying the term $\mathbf{u}' \cdot \nabla \theta'$ from eq. (5) by θ' and integrating over the
300 volume V gives:

$$\int_V \theta' \mathbf{u}' \cdot \nabla \theta' dV = \frac{1}{2} \int_V \mathbf{u}' \cdot \nabla \theta'^2 dV = \int_V \nabla \cdot \left(\mathbf{u}' \frac{\theta'^2}{2} \right) dV = \oint_{\partial V} \mathbf{u}' \cdot \mathbf{n} \frac{\theta'^2}{2} dS = 0, \quad (13)$$

301 where the last equality makes use of the no mass flux condition through the boundaries, and where
302 \mathbf{n} is the outward normal to the volume V . Similarly, the advection of the temperature anomaly by
303 the mean flow is zero when integrated on the volume because of the no mass flux condition:

$$\int_V \theta' \bar{\mathbf{u}} \cdot \nabla \theta' dV = 0. \quad (14)$$

304 The term involving the mean temperature gradient does not a priori vanish when volume inte-
305 grated, therefore, the integral on the volume of the temperature variance equation is:

$$\frac{1}{2} \frac{\partial \int_V \theta'^2 dV}{\partial t} = - \int_V \theta' \mathbf{u}' \cdot \nabla \bar{\theta} dV + \int_V \theta' D'_\theta dV + \int_V \overline{\theta' \mathbf{u}' \cdot \nabla \theta'} dV \quad (15)$$

306 The last term on the rhs is not zero when volume integrated but its time average is zero (because
 307 $\overline{\theta'} = 0$). The second term on the rhs is generally negative because positive anomalies of temper-
 308 ature are correlated with negative values of diffusion. The first term of the rhs can be described
 309 as a measure of the turbulent flux of θ' in the mean temperature gradient direction. It acts to
 310 increase (decrease) the total variance when positive (negative) temperature anomalies are fluxed
 311 in the direction opposite to the mean temperature gradient. It is the only source of temperature
 312 variance in our setup (when time averaged). This term has been used in many studies to diag-
 313 nose regions where baroclinic instability adds temperature variance to the flow (see for instance:
 314 Colin de Verdière and Huck 1999; Huck et al. 1999).

315 Using Parseval's theorem, it is possible to link the volume integral of the temperature variance
 316 terms with the frequency integral of the corresponding transfers. Indeed, using Eqs. (10) and (13)
 317 we have:

$$\Pi_{\text{turb}}(\omega_{\min}) = \int_{\omega_{\min}}^{\omega_{\max}} \text{Tr}_{\text{turb}}(\omega') d\omega' = 0, \quad (16)$$

318 the total flux of temperature variance made by the turbulent terms is zero. The role of the turbulent
 319 terms is to redistribute the temperature variance among different frequencies. From the fact that
 320 the term involving the mean temperature does not vanish, we deduce that the total flux made by
 321 the mean flow is not zero:

$$\Pi_{\text{mean}}(\omega_{\min}) = \int_{\omega_{\min}}^{\omega_{\max}} \text{Tr}_{\text{mean}}(\omega') d\omega' \neq 0. \quad (17)$$

322 Then, from Eq. (12) and Eq. (16), the total flux of variance from the mean flow is equal to the
 323 opposite of the total diffusive flux:

$$\Pi_{\text{mean}}(\omega_{\min}) = -\Pi_{\text{diss}}(\omega_{\min}) \quad (18)$$

324 *c. Application to an eddy-permitting experiment*

325 In this section we apply the diagnostics from the two previous subsections to the MITgcm nu-
326 merical simulations described in Section 2.

327 To calculate the fluxes we use a 200-year run with time average outputs every 20 days. The output
328 sampling rate needs to be large enough to resolve high frequencies. No significant changes were
329 found between 20 days and higher output frequencies (not shown). Figure 5 shows the tempera-
330 ture variance fluxes $\Pi_{\text{mean}}(\omega)$, $\Pi_{\text{turb}}(\omega)$ and $\Pi_{\text{diss}}(\omega)$. As expected from Eq. (16), $\Pi_{\text{turb}}(\omega_{\text{min}})$ is
331 zero and $\Pi_{\text{diss}}(\omega_{\text{min}}) = -\Pi_{\text{mean}}(\omega_{\text{min}})$. Π_{mean} is positive and increases toward lower frequencies
332 showing that the mean flow adds temperature variance. On the contrary, $\Pi_{\text{diss}}(\omega)$ is always neg-
333 ative and decreases toward lower frequencies because dissipation removes temperature variance.
334 $\Pi_{\text{turb}}(\omega)$ increases toward low-frequencies and then decreases, clearly establishing that nonlinear
335 terms are a sink of temperature variance for frequencies approximately smaller than $2\pi/3.5 \text{ yr}^{-1}$
336 and a source of variance for frequencies larger than $2\pi/3.5 \text{ yr}^{-1}$. This variation of the direction
337 of the turbulent transfer of temperature with frequency is the central result of this study.

338 This allows us to define High-Frequencies (HF) as being larger than $2\pi/3.5 \text{ yr}^{-1}$ and Low-
339 Frequencies (LF) as being smaller than $2\pi/3.5 \text{ yr}^{-1}$. This definition allows us to robustly sep-
340 arate the meso-scale eddy turbulence (HF) from the multidecadal mode of variability described in
341 section c. $\omega_{\text{mid}} \equiv 2\pi/3.5 \text{ yr}^{-1}$ is the maximum of $\Pi_{\text{turb}}(\omega)$; thus by definition, turbulent trans-
342 fers are a source term in HF while they are a sink in LF. The slope of Π_{mean} is larger at LF than
343 at HF, suggesting that the flux of temperature variance from the mean flow is larger for LF than
344 for HF. On the contrary, the slope of Π_{diss} is larger for HF than for LF, suggesting that dissi-
345 pation of temperature variance is more important for HF than for LF. An excess of temperature
346 variance is created at low frequencies by instability of the mean flow, transferred to high frequen-

347 cies where it is dissipated. An alternative and equivalent definition for HF and LF could then be
 348 that, HF are frequencies for which the temperature variance total transfer from the mean flow (i.e.
 349 $\Pi_{mean}(\omega_{min}) - \Pi_{mean}(\omega_{mid})$) is smaller than the removal of temperature variance by the dissipa-
 350 tion (i.e. $|\Pi_{diss}(\omega_{min}) - \Pi_{diss}(\omega_{mid})|$ with $|\cdot|$ the absolute value) while the opposite is true for LF.
 351 Figure 6 is a schematic description of the fluxes shown in Figure 5 between the HF and LF. All
 352 fluxes are expressed as a percentage of the total flux from the mean flow i.e. $\Pi_{mean}(\omega_{min})$. The
 353 transfer of temperature variance from LF to HF by turbulent terms represents 44% of the total flux
 354 by the mean flow. 79% of the variance from the mean flow is added at LF while 65% is removed
 355 by the dissipation at HF. The main pathway of the temperature variance is clearly from the mean
 356 flow LF to the HF dissipation. In other words, since LF are mainly due to the multidecadal mode
 357 (see Figure 2) and the source of variability of the mode is the mean temperature gradient, this
 358 source is mainly balanced by the meso-scale eddy turbulence acting as a sink of variance and to a
 359 lesser extent by LF dissipation. The main source of variance for the meso-scale eddy turbulence
 360 is the multidecadal mode and to a lesser extent the mean temperature gradient. These sources of
 361 HF temperature variability are balanced by the HF dissipation.

362 4. Spatial pattern of the temperature variance transfer

363 In this section we show how the different terms of the temperature budget act on the low-
 364 frequency variability. To this end we split the temperature into time mean plus low-frequency
 365 (θ_{LF}) plus high-frequency (θ_{HF}) parts:

$$\theta = \bar{\theta} + \theta_{LF} + \theta_{HF} \quad (19)$$

366 we use a low-pass filter noted $\langle \cdot \rangle$ so that $\langle \theta \rangle = \bar{\theta} + \theta_{LF}$ and obtain θ_{HF} as $\theta_{HF} = \theta - \langle \theta \rangle$.

367 The cutoff period for the Butterworth low-pass filter is chosen to be 3.5 years to match the results

368 from the previous section. In this section, the effect of HF on LF is calculated as a remainder,
 369 as will become clear below. This remainder allows us to use smaller output frequency (100 days
 370 average in this section) which significantly simplifies the computation presented below and allows
 371 the study of a longer run (300 years).

372 *a. Low-frequency temperature variance budget*

373 To obtain an evolution equation for θ_{LF} , we first write the time mean of the temperature equation:

$$\bar{\mathbf{u}} \cdot \nabla \bar{\theta} + \overline{(\mathbf{u}_{LF} + \mathbf{u}_{HF}) \cdot \nabla (\theta_{LF} + \theta_{HF})} = \bar{D} + G \quad (20)$$

374 Using (19) and subtracting Eq. (20) from the temperature equation (3), applying the low-pass
 375 filter, multiplying by θ_{LF} and volume integrating gives the low-frequency temperature variance
 376 budget :

$$\frac{1}{2} \frac{\partial}{\partial t} \int_V \theta_{LF}^2 dV = V_{\text{mean}} + V_{\text{diss}} + V_{\text{HF}} \quad (21)$$

377 where:

$$V_{\text{term}} = \int_V v_{\text{term}} dV \quad (22)$$

378 with term either mean, diss or HF and:

$$v_{\text{mean}} = -\theta_{LF} \mathbf{u}_{LF} \cdot \nabla \bar{\theta} \quad (23)$$

379

$$v_{\text{diss}} = \theta_{LF} D_{LF} \quad (24)$$

380

$$v_{\text{HF}} = -\theta_{LF} \langle \mathbf{u}_{LF} \cdot \nabla \theta_{HF} \rangle - \theta_{LF} \langle \mathbf{u}_{HF} \cdot \nabla \theta_{LF} \rangle - \theta_{LF} \langle \mathbf{u}_{HF} \cdot \nabla \theta_{HF} \rangle \\ + \theta_{LF} \overline{(\mathbf{u}_{HF} + \mathbf{u}_{LF}) \cdot \nabla (\theta_{HF} + \theta_{LF})} \quad (25)$$

381 V_{diss} is interpreted as the effect of the parameterised diffusion and convection, V_{mean} as the mean
 382 flow forcing. In v_{HF} , terms involving a time mean and a HF term disappear when low-pass fil-
 383 tered. None of the terms of v_{HF} can a priori be ruled out; however we have checked, using higher

384 frequency outputs on a shorter length simulation, that all terms involving only one HF can be
 385 neglected so that:

$$V_{HF} \approx \int_V \left(-\theta_{LF} \langle \mathbf{u}_{HF} \cdot \nabla \theta_{HF} \rangle + \theta_{LF} \overline{\mathbf{u}_{HF} \cdot \nabla \theta_{HF}} + \theta_{LF} \overline{\mathbf{u}_{LF} \cdot \nabla \theta_{LF}} \right) dV. \quad (26)$$

386 V_{HF} is thus interpreted as the influence of high-frequency motions on low-frequency temperature
 387 variance. In practice V_{HF} is computed as the remainder of all other terms, v_{mean} is calculated from
 388 the values of θ_{LF} , \mathbf{u}_{LF} and $\bar{\theta}$ and v_{diss} from the values of D_{LF} and θ_{LF} . Each term of Eq. (21) is
 389 shown in figure 7. The main equilibrium is between the forcing by V_{mean} and the dissipation by
 390 both V_{HF} and V_{diss} . High levels of LF forcing are correlated with high levels of LF dissipation:
 391 the (time) correlation coefficient is -0.87 between V_{mean} and V_{diss} and -0.85 between V_{mean} and
 392 V_{HF} . Note that the two correlations are similar but most of the variability is taken up by V_{HF} . The
 393 negative correlation between V_{mean} and V_{diss} and between V_{mean} and V_{HF} is because LF temperature
 394 gradients and meso-scale activity increase with LF forcing. On the same figure is shown the real
 395 and imaginary part of the temperature leading CEOF PC calculated in section 3. The correlation
 396 coefficient between the imaginary part PC and V_{diss} , V_{mean} and V_{HF} is small: respectively -0.16,
 397 0.01, and 0.09 while it is much larger with the PC real part: respectively 0.66, -0.62 and 0.60. The
 398 real part of the PC and by construction the AMOC strength time variation are thus approximately
 399 in phase with the LF dissipation, the LF NL transfer toward HF and the LF mean flow forcing. This
 400 is explained by the fact that a stronger AMOC is associated with increased temperature gradients
 401 and thus with a larger LF mean flow forcing, LF dissipation and with a stronger eddy field. The
 402 lagged correlation (see Fig. 8) between PC_{re} and V_{HF} , V_{mean} and V_{diss} shows that PC_{re} is close to
 403 be in phase with the three latter. There is however a small time lag of respectively -1.1 and -0.6
 404 year between V_{diss} and PC_{re} and between V_{mean} and PC_{re} while V_{HF} is almost exactly in phase
 405 with PC_{re} . The fact that V_{HF} is lagging the two other terms from 0.6 to 1.1 year is not surprising

406 because of the finite growth time-scale of eddy turbulence compared to the instantaneous action of
407 the parameterized dissipation.

408 To better understand the the spatial distribution of the V_{HF} term, we first calculate the vertical
409 average over the water column of v_{HF} , that is:

$$V_{HF}^{int} = \frac{1}{H} \int_{z=-H}^0 v_{HF} dz \quad (27)$$

410 where H is the total depth. Then, to analyse its temporal variation, we time average V_{HF}^{int} following
411 the sign of the PC's real part. The PC's real part is used rather than the imaginary part because it
412 correlates (positively) with V_{HF} (see last paragraph). The time average of V_{HF}^{int} on all t satisfying
413 $PC_{re}(t) \geq 0$ and all t satisfying $PC_{re}(t) < 0$ is shown on the two panels of figure 9. Note that
414 $PC_{re}(t)$ correlates very well with the MOC strength so that positive values of $PC_{re}(t)$ correspond
415 to a positive MOC anomaly (see subsection 3.c). Large negative values of V_{HF}^{int} are mostly located
416 in the North-West quadrant of the basin and follow large gradients of temperature created by the
417 low-frequency variability. Temperature fronts created by the low-frequency variability are unstable
418 and eroded by the subsequent eddies associated with high-frequencies. As first shown in the last
419 section, the high-frequency part of the temperature variance is mostly forced by the low-frequency
420 part (44% vs 21% in figure 6), explaining why the spatial location of V_{HF}^{int} is moving with time (Fig.
421 9). Indeed if the only source of meso-scale eddies was the time mean temperature gradients, the
422 location and intensity of the meso-scale field would remain constant in time. Volume-integrating
423 the time-average of V_{HF}^{int} reveals that the quantity of eddy induced dissipation occurring when
424 $PC_{re} > 0$ or $PC_{re} < 0$ is of the same order of magnitude with respectively 43% and 57% of the
425 total eddy induced dissipation.

426 *b. Propagation of the temperature anomaly*

427 The propagation of the temperature anomaly is usually explained (e.g. Sévellec and Fedorov
 428 (2013)) as the result of the advection of the time mean temperature by the anomalous velocities.
 429 The purpose of this subsection is to test this explanation and more broadly to understand what
 430 terms drive the oscillation captured by the temperature leading CEOF shown in figure 1. In partic-
 431 ular, we want to understand if the HF field plays a role in the LF temperature propagation.
 432 To this end, we derive below a diagnostic that allows us to evaluate the contribution of each term
 433 from the temperature anomaly budget (5) in the propagation of the leading CEOF temperature
 434 anomaly. We first calculate the linear regression of the LF temperature budget (Eq. (5)) on the real
 435 and imaginary parts of the leading CEOF's PC (see formula (1)) to obtain a separate equation for
 436 the time evolution of the real (θ_{LF}^{re}) and imaginary (θ_{LF}^{im}) part of the CEOF:

$$\left[\frac{\partial \theta_{LF}}{\partial t}\right]^{re} = -[\bar{\mathbf{u}} \cdot \nabla \theta_{LF}]^{re} - [\mathbf{u}_{LF} \cdot \nabla \bar{\theta}]^{re} - [\mathbf{u}_{LF} \cdot \nabla \theta_{LF}]^{re} + [D_{LF}]^{re} + [G_{HF}]^{re} \quad (28)$$

437 where $[\cdot]^{re}$ is the linear regression against the real part of the first CEOF PC and G_{HF} is the effect
 438 of high frequencies on low frequency temperature ($\int_V \theta_{LF} G_{HF} dV = V_{HF}$). The linear regression
 439 is given by:

$$[A(x, y, z, t)]^{re} = \frac{\int_0^T A(x, y, z, t) \text{PC}_{re}(t) dt}{\int_0^T (\text{PC}_{re}(t))^2 dt} \quad (29)$$

440 where A is any of the terms in Eq. (28) and T the length of the time series. We proceed the same
 441 way for the imaginary part:

$$\left[\frac{\partial \theta_{LF}}{\partial t}\right]^{im} = -[\bar{\mathbf{u}} \cdot \nabla \theta_{LF}]^{im} - [\mathbf{u}_{LF} \cdot \nabla \bar{\theta}]^{im} - [\mathbf{u}_{LF} \cdot \nabla \theta_{LF}]^{im} + [D_{LF}]^{im} + [G_{HF}]^{im} \quad (30)$$

442 where $[\cdot]^{im}$ is the regression against the imaginary part of the first CEOF PC, using Eq. (29) but
 443 with PC_{im} instead of PC_{re} . Following figure 1 the oscillation steps are $re \rightarrow im \rightarrow -re \rightarrow -im \rightarrow$
 444 re . The two last transitions are the same as the first two except for their sign and we can thus restrict

445 ourselves to the former. To understand what term is a positive or a negative contributor to $re \rightarrow im$
 446 ($im \rightarrow -re$) we volume-average the product of $[\frac{\partial \theta_{LF}}{\partial t}]^{re}$ and each term of Eq. (28) ($[\frac{\partial \theta_{LF}}{\partial t}]^{im}$ and
 447 each term of Eq. (30)). When the volume-average of the product is positive (negative) the term
 448 positively (negatively) contributes to the oscillation. All values are normalized by the volume
 449 average of $([\frac{\partial \theta_{LF}}{\partial t}]^{re})^2$ for Eq. (28) and by the volume average of $([\frac{\partial \theta_{LF}}{\partial t}]^{im})^2$ for Eq. (30) and
 450 shown in table 1.

451 In agreement with previous descriptions of this LF mode (for instance in Sévellec and Fedorov
 452 (2013)), the propagation of the large-scale temperature anomaly is mainly due to the term $\mathbf{u}_{LF} \cdot \nabla \bar{\theta}$.
 453 The LF temperature anomaly is associated with anomalous LF velocities that in turn advect mean
 454 temperature in a way that creates this propagation. We show, in figure 10, that $\bar{\mathbf{u}} \cdot \nabla \theta_{LF}$ resists the
 455 propagation. To understand why the term involving $\bar{\mathbf{u}} \cdot \nabla \theta_{LF}$ is opposite to $\mathbf{u}_{LF} \cdot \nabla \bar{\theta}$ we show, in
 456 figure 10, the two terms regressed against the real and imaginary parts of the 1st CEOF PC. It is
 457 seen that, for both real and imaginary parts we have:

$$\mathbf{u}_{LF} \cdot \nabla \bar{\theta} \propto -\bar{\mathbf{u}} \cdot \nabla \theta_{LF}, \quad (31)$$

458 where \propto is the proportionality symbol. This is due to the “non-Doppler shift” (Rossby 1939; Held
 459 1983; Killworth et al. 1997; Liu 1999) which states that the geostrophic self advection and the
 460 mean advection exactly cancel each other when the mean flow and the anomaly have the same
 461 vertical structure.

462 The contributions from the remaining terms ($\mathbf{u}_{LF} \cdot \nabla \theta_{LF}$, diffusion and eddy turbulence) are
 463 much smaller. Thus, eddy turbulence that appears when eddy-permitting resolution are used does
 464 not significantly modify the oscillatory mechanism that was previously described in low resolution
 465 studies (Te Raa and Dijkstra 2002; Sévellec and Fedorov 2013).

466 5. Conclusion

467 In this article we seek to better understand the interaction between high and low-frequency
468 variability in the ocean, i.e., between a multidecadal mode of variability and meso-scale eddy tur-
469 bulence. To this end, we study an idealized configuration of the North Atlantic using an OGCM
470 at eddy-permitting resolution (20km) that allows the coexistence of a multidecadal mode of vari-
471 ability and high-frequency meso-scale variability. In agreement with many other studies of this
472 mode (Colin de Verdière and Huck 1999; Sévellec and Huck 2015), the multidecadal mode is
473 sustained by temperature variance drawn from the time mean circulation. This mode has a domi-
474 nant period of 42 years and consists of large-scale temperature anomalies propagating northward
475 in the Northern half of the basin. The high-frequency variability is associated with meso-scale
476 eddy turbulence driven by temperature variance drawn from both the time-mean flow and the low-
477 frequency large-scale mode. A new diagnostic of temperature variance fluxes in frequency space
478 reveals that high-frequencies are a sink of temperature variance for the low-frequencies. At low
479 and high frequencies the positive flux of temperature variance from the mean flow is not equal to
480 the opposite of the diffusive flux: a turbulent flux of temperature variance from LF to HF balances
481 the budget for the LF and HF temperature variance reservoirs. Indeed, in our setup, the temper-
482 ature variance flux from the mean flow is more than two times larger than the dissipation at low
483 frequencies. Writing the temperature variance equation for the LF allows visualization of the term
484 contributing to the high and low frequency variance. This term that we attribute to the overall
485 effect of meso-scale eddies, follows the LF temperature gradient in the western half of the basin
486 showing that HF erodes the LF fronts. Regarding the propagation of the LF temperature anomaly
487 we have shown that the eddy term plays no significant role. The main driver of the propagation
488 is the advection of time mean temperature by LF anomalous velocities: $\mathbf{u}_{LF} \cdot \nabla \bar{\theta}$ mainly counter-

489 acted by the advection of anomalous LF temperature by time mean velocities: $\bar{\mathbf{u}} \cdot \nabla \theta_{LF}$. Results
490 from O'Rourke et al. (2018); Sérazin et al. (2018); Martin et al. (2020) have shown that surface
491 KE undergoes an inverse cascade of energy in both spatial and temporal space. Our results are
492 not necessarily in contradiction with these studies because under the QG approximation, the tem-
493 perature variance behaves closely to QG Available Potential Energy which is known to follow a
494 direct cascade in both spatial and temporal space (Arbic et al. 2014). However in our simulation
495 the QG approximation does not hold (because isotherms outcrop at the surface in the Northern
496 half of the basin) and the direction of the APE cascade therefore remains unclear. The large-scale
497 low-frequency variability is primarily seen in temperature and has very little KE (because its scale
498 is much larger than the deformation radius) which makes it more relevant to an analysis in terms
499 of temperature variance.

500 LaCasce and Pedlosky (2004); Isachsen et al. (2007) have shown that propagating Rossby waves
501 are prone to meso-scale instabilities. At high latitudes, where Rossby waves phase speed is slower
502 than at lower latitudes, their studies suggest that meso-scale eddies prevent Rossby waves from
503 reaching the western boundary. Given that the large scale temperature anomaly that we see in our
504 simulation could be described as a Rossby wave modified by the effect of the mean flow, the same
505 mechanism is at play in our study except that the large scale variability is continuously forced by
506 the large scale baroclinic instability (Colin de Verdière and Huck 1999). This baroclinic insta-
507 bility compensates for the transfer to HF made by meso-scale eddies (as shown by the schematic
508 in figure 6). As explained in the introduction, it was found in Huck et al. (2015), that the range
509 of K_v allowing a low frequency oscillation is larger at high than at low resolution. Huck et al.
510 (2015) then suggested that this could be explained by the fact that meso-scale eddies were acting
511 as a forcing for the LF mode at high resolution. Because we showed that the temperature variance
512 transfer is directed toward high frequencies, this wider range of K_v is however probably due to a

513 smaller effective diffusivity in the high resolution run rather than due to a forcing by meso-scale
514 eddies. Indeed the mode is known to be sensitive to the amount of diffusivity (Huck and Vallis
515 2001) and the total effective diffusivity is hard to assess at eddy-permitting resolution.
516 As shown by previous studies (e.g. Huck et al. (2015)) the use of a single hemispheric basin al-
517 lows us to capture the essential features of the large scale mode in a simple framework. Indeed,
518 the vertical structure, energy source, period of the large scale mode found in this study are also
519 seen in realistic configuration of the North Atlantic and world ocean (Sévellec and Fedorov 2013;
520 Muir and Fedorov 2017; Arzel et al. 2018).

521 However, several limitations arise from the omission of the full basin. Indeed it is now conjectured
522 that the effect of wind over the Southern Ocean needs to be taken into account to obtain a realistic
523 stratification as well as realistic values of K_v (Toggweiler and Samuels 1998; Gnanadesikan 1999;
524 Vallis 2000; Nikurashin and Vallis 2012). The effect of K_v on our results will be reported in a
525 separate study where we show that increasing K_v strengthens the eddy field and thus the transfer
526 of LF temperature variance to HF. The mode eventually disappears for unrealistically large values
527 of K_v ($\approx 1 \times 10^{-3} \text{ m}^2 \text{ s}^{-1}$). In our setup, the eddy-field is of primary importance for the large-scale
528 low-frequency mode because it represents more than 50% of the LF temperature variance destruc-
529 tion. With higher resolution and subsequent lower parameterised diffusion, virtually all the low
530 frequency dissipation may be performed by the eddy field. Thus, future studies should adequately
531 simulate eddies by allowing a more realistic stratification through the effect of wind forcing. Also,
532 wind forcing over the North Atlantic creates its own kind of low frequency variability (Berloff and
533 McWilliams 1999; Berloff et al. 2007) that might interact with the low frequency mode described
534 in this study and might modify substantially the eddy field and potentially the dissipation of the
535 low frequency mode. We do not expect a fundamental change when using eddy-resolving rather
536 than eddy-permitting resolution. Indeed, Huck et al. (2015) have shown that if the eddy field is

537 stronger at 10 km than at 20 km horizontal resolution, the large scale mode period, spatial scale and
538 mechanism remain almost unchanged. However, we can expect that the intensity of the turbulent
539 transfer of temperature variance from LF to HF will increase with increased resolution until all the
540 input of LF temperature variance by the mean flow is removed by the turbulent transfer from LF to
541 HF (i.e. the flux due to the parameterised dissipation disappears). Sérazin et al. (2018) compared
542 the surface kinetic energy inverse cascade in a $1/4^\circ$ and in a $1/12^\circ$ global simulation. They found
543 that the $1/4^\circ$ simulation resolves the main non-linear oceanic processes generating the KE inverse
544 cascade. We are thus confident that our 20 km resolution simulation also captures the essential
545 features of the non-linear oceanic processes.

546 Other limitations come from the omission of active salt tracer and freshwater forcing though it has
547 been shown in a realistic setup (Sévellec and Fedorov 2013) that the mode is largely controlled
548 by temperature variation in the upper ocean. The simulations shown here cannot be compared
549 with observations because of the idealized forcing and geometry of the basin. However, low res-
550 olution simulations (Sévellec and Fedorov 2013; Buckley et al. 2012, e.g.) have shown that the
551 low frequency variability still exists in more realistic setups. The intensity and location of the
552 meso-scale field and of the large scale mode is believed to strongly depend on the details of the
553 forcing bathymetry and coastline. The next step will thus be to study the interaction of low and
554 high frequencies in a realistic configuration of a high resolution OGCM.

555 *Acknowledgments.* This study was supported by a EU Marie Curie IF grant number 749924.
556 Numerical computations were conducted using the Pôle de Calcul Intensif pour la Mer at Ifremer,
557 Brest, France. We thank the MITgcm development group for making their model freely available.

558 **References**

- 559 Arbic, B. K., M. Müller, J. G. Richman, J. F. Shriver, A. J. Morten, R. B. Scott, G. Sérazin, and
560 T. Penduff, 2014: Geostrophic turbulence in the frequency–wavenumber domain: Eddy-driven
561 low-frequency variability. *Journal of Physical Oceanography*, **44 (8)**, 2050–2069.
- 562 Arbic, B. K., R. B. Scott, G. R. Flierl, A. J. Morten, J. G. Richman, and J. F. Shriver, 2012: Non-
563 linear cascades of surface oceanic geostrophic kinetic energy in the frequency domain. *Journal*
564 *of Physical Oceanography*, **42 (9)**, 1577–1600.
- 565 Arzel, O., and T. Huck, 2020: Contributions of atmospheric stochastic forcing and intrinsic ocean
566 modes to north atlantic ocean interdecadal variability. *Journal of Climate*, **33 (6)**, 2351–2370.
- 567 Arzel, O., T. Huck, and A. Colin de Verdière, 2006: The different nature of the interdecadal
568 variability of the thermohaline circulation under mixed and flux boundary conditions. *Journal*
569 *of physical oceanography*, **36 (9)**, 1703–1718.
- 570 Arzel, O., T. Huck, and A. Colin de Verdière, 2018: The internal generation of the atlantic ocean
571 interdecadal variability. *Journal of Climate*, **31 (16)**, 6411–6432.
- 572 Arzel, O., A. C. d. V. Verdière, and T. Huck, 2007: On the origin of interdecadal oscillations in a
573 coupled ocean atmosphere model. *Tellus A: Dynamic Meteorology and Oceanography*, **59 (3)**,
574 367–383.
- 575 Ba, J., and Coauthors, 2014: A multi-model comparison of atlantic multidecadal variability. *Cli-*
576 *mate dynamics*, **43 (9-10)**, 2333–2348.
- 577 Berloff, P., A. M. C. Hogg, and W. Dewar, 2007: The turbulent oscillator: A mechanism of low-
578 frequency variability of the wind-driven ocean gyres. *Journal of Physical Oceanography*, **37 (9)**,
579 2363–2386.

- 580 Berloff, P. S., and J. C. McWilliams, 1999: Large-scale, low-frequency variability in wind-driven
581 ocean gyres. *Journal of Physical Oceanography*, **29** (8), 1925–1949.
- 582 Bjerknes, J., 1964: Atlantic Air-Sea Interaction. *Advances in Geophysics*, H. E. Landsberg, and
583 J. Van Mieghem, Eds., Vol. 10, Elsevier.
- 584 Buckley, M. W., D. Ferreira, J.-M. Campin, J. Marshall, and R. Tulloch, 2012: On the relation-
585 ship between decadal buoyancy anomalies and variability of the atlantic meridional overturning
586 circulation. *Journal of Climate*, **25** (23), 8009–8030.
- 587 Chen, F., and M. Ghil, 1996: Interdecadal variability in a hybrid coupled ocean-atmosphere model.
588 *Journal of physical oceanography*, **26** (8), 1561–1578.
- 589 Cheng, W., R. Bleck, and C. Rooth, 2004: Multi-decadal thermohaline variability in an ocean–
590 atmosphere general circulation model. *Climate dynamics*, **22** (6-7), 573–590.
- 591 Chylek, P., C. K. Folland, H. A. Dijkstra, G. Lesins, and M. K. Dubey, 2011: Ice-core data ev-
592 idence for a prominent near 20 year time-scale of the Atlantic Multidecadal Oscillation. *Geo-*
593 *physical Research Letters*, **38** (13).
- 594 Clement, A., K. Bellomo, L. N. Murphy, M. A. Cane, T. Mauritsen, G. Radel, and B. Stevens,
595 2015: The Atlantic Multidecadal Oscillation without a role for ocean circulation. *Science*,
596 **350** (6258), 320–324.
- 597 Colin de Verdière, A., and T. Huck, 1999: Baroclinic instability: An oceanic wavemaker for
598 interdecadal variability. *Journal of Physical Oceanography*, **29** (5), 893–910.
- 599 Danabasoglu, G., S. G. Yeager, Y.-O. Kwon, J. J. Tribbia, A. S. Phillips, and J. W. Hurrell,
600 2012: Variability of the atlantic meridional overturning circulation in ccsm4. *Journal of cli-*
601 *mate*, **25** (15), 5153–5172.

- 602 Delworth, T., S. Manabe, and R. J. Stouffer, 1993: Interdecadal variations of the thermohaline
603 circulation in a coupled ocean-atmosphere model. *Journal of Climate*, **6 (11)**, 1993–2011.
- 604 Delworth, T. L., and R. J. Greatbatch, 2000: Multidecadal thermohaline circulation variability
605 driven by atmospheric surface flux forcing. *Journal of Climate*, **13 (9)**, 1481–1495.
- 606 Delworth, T. L., and M. E. Mann, 2000: Observed and simulated multidecadal variability in the
607 northern hemisphere. *Climate Dynamics*, **16 (9)**, 661–676.
- 608 Deser, C., M. A. Alexander, S.-P. Xie, and A. S. Phillips, 2010: Sea surface temperature variability:
609 Patterns and mechanisms. *Annual review of marine science*, **2**, 115–143.
- 610 Dijkstra, H. A., and M. Ghil, 2005: Low-frequency variability of the large-scale ocean circulation:
611 A dynamical systems approach. *Reviews of Geophysics*, **43 (3)**.
- 612 Dong, B., and R. T. Sutton, 2005: Mechanism of interdecadal thermohaline circulation variability
613 in a coupled ocean–atmosphere gcm. *Journal of climate*, **18 (8)**, 1117–1135.
- 614 Drews, A., and R. J. Greatbatch, 2017: Evolution of the atlantic multidecadal variability in a model
615 with an improved north atlantic current. *Journal of Climate*, **30 (14)**, 5491–5512.
- 616 Enfield, D. B., A. M. Mestas-Nuñez, and P. J. Trimble, 2001: The Atlantic Multidecadal Oscil-
617 lation and its relation to rainfall and river flows in the continental U.S. *Geophysical Research*
618 *Letters*, **28 (10)**, 2077–2080, doi:10.1029/2000GL012745, URL [http://doi.wiley.com/10.1029/](http://doi.wiley.com/10.1029/2000GL012745)
619 [2000GL012745](http://doi.wiley.com/10.1029/2000GL012745).
- 620 Folland, C., D. Parker, and F. Kates, 1984: Worldwide marine temperature fluctuations 1856–
621 1981. *Nature*, **310 (5979)**, 670.
- 622 Folland, C. K., T. N. Palmer, and D. E. Parker, 1986: Sahel rainfall and worldwide sea tempera-
623 tures, 1901-85. *Nature*, **320 (6063)**, 602.

- 624 Frankcombe, L. M., H. A. Dijkstra, and A. Von der Heydt, 2009: Noise-induced multidecadal vari-
625 ability in the North Atlantic: Excitation of normal modes. *Journal of Physical Oceanography*,
626 **39** (1), 220–233.
- 627 Frankignoul, C., and K. Hasselmann, 1977: Stochastic climate models, Part II Application to
628 sea-surface temperature anomalies and thermocline variability. *Tellus*, **29** (4), 289–305.
- 629 Gastineau, G., J. Mignot, O. Arzel, and T. Huck, 2018: North atlantic ocean internal decadal
630 variability: Role of the mean state and ocean-atmosphere coupling. *Journal of Geophysical*
631 *Research: Oceans*, **123** (8), 5949–5970.
- 632 Gent, P. R., and J. C. McWilliams, 1990: Isopycnal mixing in ocean circulation models. *Journal of*
633 *Physical Oceanography*, **20** (1), 150–155.
- 634 Gnanadesikan, A., 1999: A simple predictive model for the structure of the oceanic pycnocline.
635 *Science*, **283** (5410), 2077–2079.
- 636 Greatbatch, R. J., and S. Zhang, 1995: An interdecadal oscillation in an idealized ocean basin
637 forced by constant heat flux. *Journal of climate*, **8** (1), 81–91.
- 638 Hasselmann, K., 1976: Stochastic climate models part I. Theory. *tellus*, **28** (6), 473–485.
- 639 Held, I. M., 1983: Stationary and quasi-stationary eddies in the extratropical troposphere: Theory.
640 *Large-scale dynamical processes in the atmosphere*, 127–168.
- 641 Huang, R. X., and R. L. Chou, 1994: Parameter sensitivity study of the saline circulation. *Climate*
642 *Dynamics*, **9** (8), 391–409.
- 643 Huck, T., O. Arzel, and F. Sévellec, 2015: Multidecadal variability of the overturning circulation
644 in presence of eddy turbulence. *Journal of Physical Oceanography*, **45** (1), 157–173.

- 645 Huck, T., A. Colin de Verdière, and A. J. Weaver, 1999: Interdecadal variability of the ther-
646 mohaline circulation in box-ocean models forced by fixed surface fluxes. *Journal of physical*
647 *oceanography*, **29** (5), 865–892.
- 648 Huck, T., and G. K. Vallis, 2001: Linear stability analysis of the three-dimensional thermally-
649 driven ocean circulation: application to interdecadal oscillations. *Tellus A*, **53** (4), 526–545.
- 650 Huck, T., G. K. Vallis, and A. Colin de Verdière, 2001: On the robustness of the interdecadal
651 modes of the thermohaline circulation. *Journal of climate*, **14** (5), 940–963.
- 652 Isachsen, P., J. H. LaCasce, and J. Pedlosky, 2007: Rossby wave instability and apparent phase
653 speeds in large ocean basins. *Journal of physical oceanography*, **37** (5), 1177–1191.
- 654 Jamet, Q., T. Huck, O. Arzel, J.-M. Campin, and A. Colin de Verdière, 2016: Oceanic
655 control of multidecadal variability in an idealized coupled GCM. *Climate Dynamics*,
656 **46** (9-10), 3079–3095, doi:10.1007/s00382-015-2754-3, URL [http://link.springer.com/10.](http://link.springer.com/10.1007/s00382-015-2754-3)
657 [1007/s00382-015-2754-3](http://link.springer.com/10.1007/s00382-015-2754-3).
- 658 Juricke, S., T. N. Palmer, and L. Zanna, 2017: Stochastic subgrid-scale ocean mixing: impacts on
659 low-frequency variability. *Journal of Climate*, **30** (13), 4997–5019.
- 660 Keenlyside, N. S., J. Ba, J. Mecking, N.-E. Omrani, M. Latif, R. Zhang, and R. Msadek, 2016:
661 North atlantic multi-decadal variability—mechanisms and predictability. *Climate change: Mul-*
662 *tidecadal and beyond*, World Scientific, 141–157.
- 663 Killworth, P. D., D. B. Chelton, and R. A. de Szoek, 1997: The speed of observed and theoretical
664 long extratropical planetary waves. *Journal of Physical Oceanography*, **27** (9), 1946–1966.

- 665 Kim, W. M., S. Yeager, P. Chang, and G. Danabasoglu, 2018: Low-frequency north atlantic climate
666 variability in the community earth system model large ensemble. *Journal of Climate*, **31** (2),
667 787–813.
- 668 Knudsen, M. F., M.-S. Seidenkrantz, B. H. Jacobsen, and A. Kuijpers, 2011: Tracking the Atlantic
669 Multidecadal Oscillation through the last 8,000 years. *Nature communications*, **2**, 178.
- 670 Kushnir, Y., 1994: Interdecadal variations in North Atlantic sea surface temperature and associated
671 atmospheric conditions. *Journal of Climate*, **7** (1), 141–157.
- 672 LaCasce, J. H., and J. Pedlosky, 2004: The instability of Rossby basin modes and the oceanic eddy
673 field. *Journal of physical oceanography*, **34** (9), 2027–2041.
- 674 Liu, Z., 1999: Planetary wave modes in the thermocline: Non-doppler-shift mode, advective mode
675 and green mode. *Quarterly Journal of the Royal Meteorological Society*, **125** (556), 1315–1339.
- 676 Marshall, J., A. Adcroft, C. Hill, L. Perelman, and C. Heisey, 1997: A finite-volume, incompress-
677 ible Navier Stokes model for studies of the ocean on parallel computers. *Journal of Geophysical*
678 *Research: Oceans*, **102** (C3), 5753–5766.
- 679 Martin, P. E., B. K. Arbic, A. McC. Hogg, A. E. Kiss, J. R. Munroe, and J. R. Blundell, 2020:
680 Frequency-domain analysis of the energy budget in an idealized, coupled, ocean-atmosphere
681 model. *Journal of Climate*, (2020).
- 682 Muir, L. C., and A. V. Fedorov, 2017: Evidence of the amoc interdecadal mode related to westward
683 propagation of temperature anomalies in cmip5 models. *Climate Dynamics*, **48** (5-6), 1517–
684 1535.

- 685 Nikurashin, M., and G. Vallis, 2012: A theory of the interhemispheric meridional overturning
686 circulation and associated stratification. *Journal of Physical Oceanography*, **42** (10), 1652–
687 1667.
- 688 O’Reilly, C. H., M. Huber, T. Woollings, and L. Zanna, 2016: The signature of low-frequency
689 oceanic forcing in the atlantic multidecadal oscillation. *Geophysical Research Letters*, **43** (6),
690 2810–2818.
- 691 O’Rourke, A. K., B. K. Arbic, and S. M. Griffies, 2018: Frequency-domain analysis of atmospher-
692 ically forced versus intrinsic ocean surface kinetic energy variability in GFDL CM2-O model
693 hierarchy. *Journal of Climate*, **31** (5), 1789–1810.
- 694 Robson, J., P. Ortega, and R. Sutton, 2016: A reversal of climatic trends in the north atlantic since
695 2005. *Nature Geoscience*, **9** (7), 513–517.
- 696 Rossby, C., 1939: Relationship between variations in the intensity of the zonal variation and the
697 displacement of the semipermanent centers of action. *Journal of Marine Research*, **2**, 38–55.
- 698 Scott, R. B., and B. K. Arbic, 2007: Spectral energy fluxes in geostrophic turbulence: Implications
699 for ocean energetics. *Journal of physical oceanography*, **37** (3), 673–688.
- 700 Sérazin, G., T. Penduff, S. Grégorio, B. Barnier, J.-M. Molines, and L. Terray, 2015: Intrinsic
701 variability of sea level from global $1/12^\circ$ ocean simulations: Spatiotemporal scales. *Journal of*
702 *Climate*, **28** (10), 4279–4292.
- 703 Sévellec, F., and A. V. Fedorov, 2013: The leading, interdecadal eigenmode of the Atlantic merid-
704 ional overturning circulation in a realistic ocean model. *Journal of Climate*, **26** (7), 2160–2183.
- 705 Sévellec, F., and T. Huck, 2015: Theoretical investigation of the atlantic multidecadal oscillation.
706 *Journal of Physical Oceanography*, **45** (9), 2189–2208.

- 707 Sévellec, F., T. Huck, M. Ben Jelloul, and J. Vialard, 2009: Nonnormal multidecadal response
708 of the thermohaline circulation induced by optimal surface salinity perturbations. *Journal of*
709 *Physical Oceanography*, **39** (4), 852–872.
- 710 Simonnet, E., and H. A. Dijkstra, 2002: Spontaneous generation of low-frequency modes of vari-
711 ability in the wind-driven ocean circulation. *Journal of physical oceanography*, **32** (6), 1747–
712 1762.
- 713 Stammer, D., 1997: Global characteristics of ocean variability estimated from regional
714 topex/poseidon altimeter measurements. *Journal of Physical Oceanography*, **27** (8), 1743–1769.
- 715 Sérazin, G., T. Penduff, B. Barnier, J.-M. Molines, B. K. Arbic, M. Muller, and L. Terray, 2018:
716 Inverse Cascades of Kinetic Energy as a Source of Intrinsic Variability: A Global OGCM Study.
717 *Journal of Physical Oceanography*, **48** (6), 1385–1408.
- 718 Te Raa, L. A., and H. A. Dijkstra, 2002: Instability of the thermohaline ocean circulation on
719 interdecadal timescales. *Journal of physical oceanography*, **32** (1), 138–160.
- 720 Toggweiler, J. R., and B. Samuels, 1998: On the ocean large-scale circulation near the limit of no
721 vertical mixing. *Journal of Physical Oceanography*, **28** (9), 1832–1852.
- 722 Vallis, G. K., 2000: Large-scale circulation and production of stratification: Effects of wind,
723 geometry, and diffusion. *Journal of Physical Oceanography*, **30** (5), 933–954.
- 724 Von Storch, H., and F. W. Zwiers, 2001: *Statistical analysis in climate research*. Cambridge uni-
725 versity press.
- 726 Watanabe, M., and H. Tatebe, 2019: Reconciling roles of sulphate aerosol forcing and internal
727 variability in Atlantic multidecadal climate changes. *Climate Dynamics*, **53** (7-8), 4651–4665,
728 publisher: Springer.

- 729 Wills, R. C., K. C. Armour, D. S. Battisti, and D. L. Hartmann, 2019: Ocean–atmosphere dynam-
730 ical coupling fundamental to the atlantic multidecadal oscillation. *Journal of Climate*, **32** (1),
731 251–272.
- 732 Zhang, R., 2017: On the persistence and coherence of subpolar sea surface temperature and salin-
733 ity anomalies associated with the Atlantic multidecadal variability. *Geophysical Research Let-*
734 *ters*, **44** (15), 7865–7875.
- 735 Zhang, R., R. Sutton, G. Danabasoglu, T. L. Delworth, W. M. Kim, J. Robson, and S. G. Yeager,
736 2016: Comment on “the atlantic multidecadal oscillation without a role for ocean circulation”.
737 *Science*, **352** (6293), 1527–1527.
- 738 Zhang, R., R. Sutton, G. Danabasoglu, Y.-O. Kwon, R. Marsh, S. G. Yeager, D. E. Amrhein, and
739 C. M. Little, 2019: A Review of the Role of the Atlantic Meridional Overturning Circulation
740 in Atlantic Multidecadal Variability and Associated Climate Impacts. *Reviews of Geophysics*,
741 **0** (ja), doi:10.1029/2019RG000644, URL [https://agupubs.onlinelibrary.wiley.com/doi/abs/10.](https://agupubs.onlinelibrary.wiley.com/doi/abs/10.1029/2019RG000644)
742 [1029/2019RG000644](https://agupubs.onlinelibrary.wiley.com/doi/abs/10.1029/2019RG000644).
- 743 Zu, Z., M. Mu, and H. A. Dijkstra, 2013: Optimal nonlinear excitation of decadal variability of the
744 North Atlantic thermohaline circulation. *Chinese journal of oceanology and limnology*, **31** (6),
745 1368–1374.

746 **LIST OF TABLES**

747 **Table 1.** Contributions to the LF evolution of temperature, computed as the volume in-
748 tegrated correlations between $[\frac{\partial\theta_{LF}}{\partial t}]^{re}$ and the rhs terms of (28), and $[\frac{\partial\theta_{LF}}{\partial t}]^{im}$
749 and Eq. (30) (“im→-re” column). For each column, values are expressed as a
750 percentage of the sum of all terms. 37

θ_{LF} budget term	re→im	im→-re
$\mathbf{u}_{LF} \cdot \nabla \bar{\theta}$	+219%	+213%
$\bar{\mathbf{u}} \cdot \nabla \theta_{LF}$	-129%	-153%
$\mathbf{u}_{LF} \cdot \nabla \theta_{LF}$	+14%	+24%
G_{HF}	-0%	+14%
D_{LF}	-4%	+2%
Σ	+100%	+100%

751 TABLE 1. Contributions to the LF evolution of temperature, computed as the volume integrated correlations
752 between $[\frac{\partial \theta_{LF}}{\partial t}]^{re}$ and the rhs terms of (28), and $[\frac{\partial \theta_{LF}}{\partial t}]^{im}$ and Eq. (30) (“im→-re” column). For each column,
753 values are expressed as a percentage of the sum of all terms.

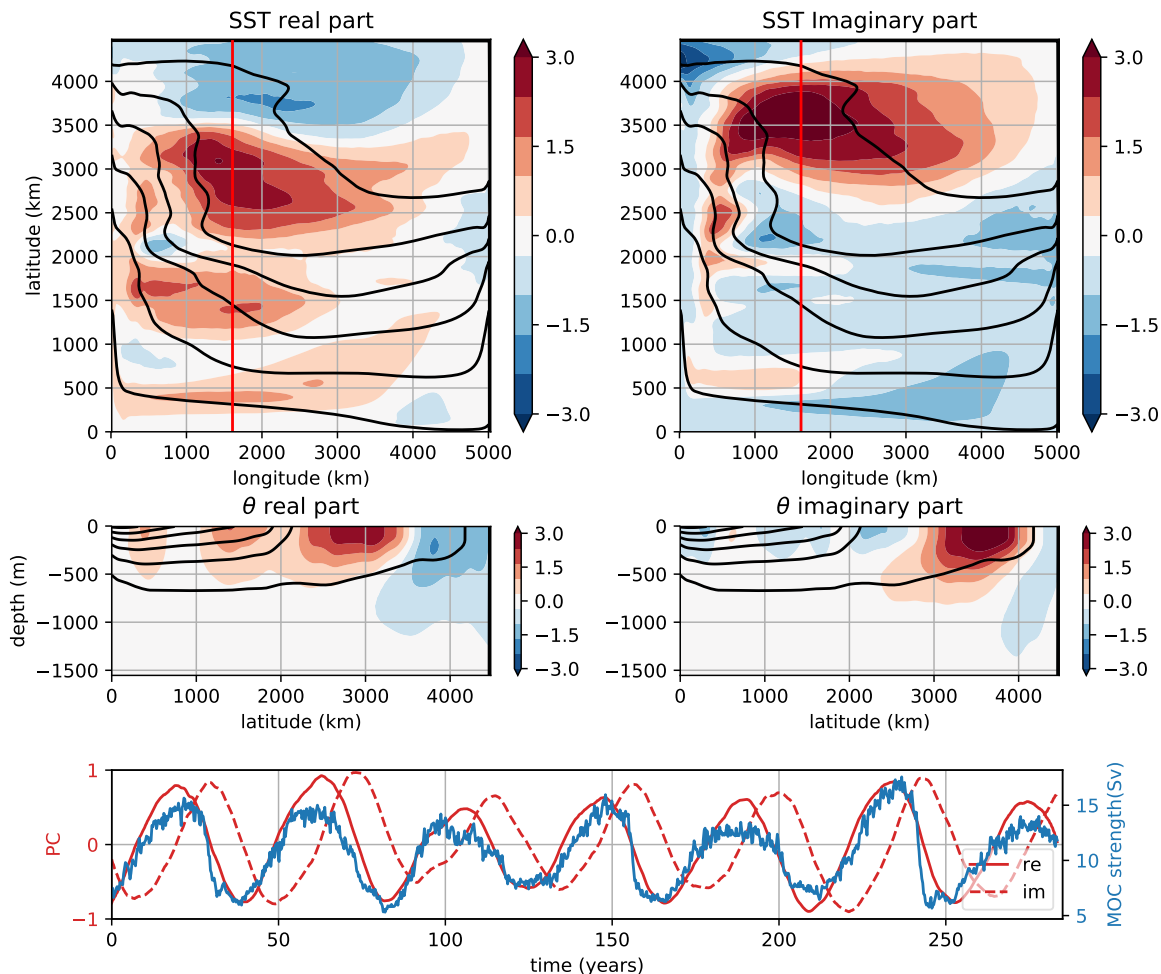
LIST OF FIGURES

- 755 **Fig. 1.** First Complex EOF calculated on 1 year averaged 3D temperature outputs, accounting for
756 60% of the variability. Top left: real part of the SST, top right imaginary part of the SST.
757 Middle left: real part of the meridional section (longitude = 1800km) shown by a red line on
758 the top left and right panels, middle right: imaginary part of the same section. Black contours
759 show isotherms of the time mean temperature. Bottom: real (red solid) and imaginary (red
760 dotted) part of the principal component of the first CEOF. The blue line shows the MOC
761 strength (in Sv) at the latitude ($y_{max} = 3500\text{km}$) and depth ($z_{max} = -500\text{m}$) where the time
762 mean MOC is maximum. 40
- 763 **Fig. 2.** Volume average of the temperature spectrum as a function of frequency calculated from 1
764 year average output over 500 years (black line) and 3 days average output over 50 years
765 (dashed black line). The largest peak and its harmonic respectively have a frequency of
766 $2\pi/42\text{ yr}^{-1}$ and $2\pi/21\text{ yr}^{-1}$ (blue vertical lines). The $2\pi/3.5\text{ yr}^{-1}$ limit between Low and
767 High frequencies (defined in subsection c) is shown with a black vertical line. MOC fre-
768 quency spectrum calculated with Welch's method on 1 year average outputs over 500 years
769 is in red. 41
- 770 **Fig. 3.** Left: standard deviation of Sea Surface Height (in m) using 3 days output on a 50 year
771 period with 2 years running average removed. Right: snapshot of the ratio of the surface
772 relative vorticity $\partial_x v - \partial_y u$ and f 42
- 773 **Fig. 4.** Left: time mean of the surface zonal velocity (m s^{-1}). Right: meridional section of the time
774 mean surface zonal velocity at longitude=1000 km (as shown by the black vertical line on
775 the left panel). 43
- 776 **Fig. 5.** Temperature variance fluxes as a function of frequency for Π_{diss} (blue), Π_{turb} (orange) and
777 Π_{mean} (green) as defined by Eq. (7), (8), (9) and (10). The vertical line at $2\pi/3.5$ years
778 corresponds to the maximum of Π_{turb} and is used to separate the High and Low-Frequencies
779 (i.e. eddy turbulence and multidecadal mode of variability). 44
- 780 **Fig. 6.** Schematic showing the temperature variance fluxes between low- and high-frequencies
781 reservoirs. All percentages are expressed with respect to the total flux of temperature vari-
782 ance from the mean flow ($\Pi_{\text{mean}}(\omega_{\text{min}})$). Direction of arrows shows direction of the fluxes.
783 Π_{diss} is in blue, Π_{mean} is in green and Π_{turb} is in orange. The sum of all arrows for each
784 reservoir is 0. 45
- 785 **Fig. 7.** Time evolution of the volume averaged low-frequency temperature variance budget. The
786 effect of mean temperature gradient V_{mean} is in green, the effect of parameterised diffusion
787 V_{diss} is in blue, the effect of high-frequencies on low-frequencies V_{HF} is in orange, and the
788 sum of all terms (equal to $\frac{1}{2} \frac{\partial}{\partial t} \int_V \theta_{\text{LF}}^2 dV$) is in red. The real and imaginary part of the leading
789 CEOF PC are shown with respectively solid and dashed black lines. 46
- 790 **Fig. 8.** Lagged correlation between the PC's real part (PC_{re}) and V_{diss} (in blue), V_{HF} (in orange)
791 and V_{mean} (in green). The lagged times (in years) for the minimum correlation between PC_{re}
792 and V_{diss} and V_{HF} ; and for the maximum correlation between PC_{re} and V_{mean} are shown with
793 three vertical lines. 47
- 794 **Fig. 9.** Effect of eddies (in $\text{K}^2 \text{s}^{-1}$) on the low-frequency temperature variance. $V_{\text{HF}}^{\text{int}}$ (see Eq. (27))
795 is time averaged on two time periods defined by the sign of the real part of the leading
796 temperature CEOF PC (see Fig. 1). Left panel: $PC_{\text{re}} \geq 0$, right panel: $PC_{\text{re}} < 0$. The sign
797 of the MOC anomaly (ΔMOC) is shown in each panel title and is the same as the PC_{re} sign.

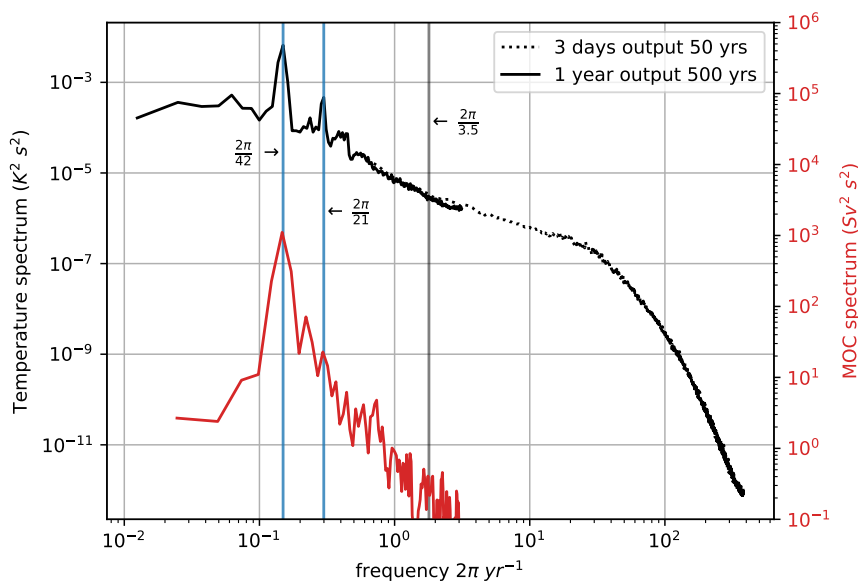
798 The superimposed black contours show the temperature averaged on the same depths and
 799 times, in red is the 4.5 K contour. V_{HF}^{int} follows the largest LF temperature gradients that
 800 appear in the western half of the basin. 48

801 **Fig. 10.** Contribution of $\mathbf{u}_{LF} \cdot \nabla \bar{\theta}$ (middle panels), $\bar{\mathbf{u}} \cdot \nabla \theta_{LF}$ (top panels) and their sum $\bar{\mathbf{u}} \cdot \nabla \theta_{LF} + \mathbf{u}_{LF} \cdot$
 802 $\nabla \bar{\theta}$ to the low-frequency temperature budget. Each term is regressed respectively against the
 803 real part (left panels) and imaginary part (right panels) of the leading CEOF PC. Note the
 804 different colorbar. Units: K s^{-1} . $\mathbf{u}_{LF} \cdot \nabla \bar{\theta}$ is partly compensated by $\bar{\mathbf{u}} \cdot \nabla \theta_{LF}$ due to the
 805 “non-Doppler shift” as explained in section 4 b. 49

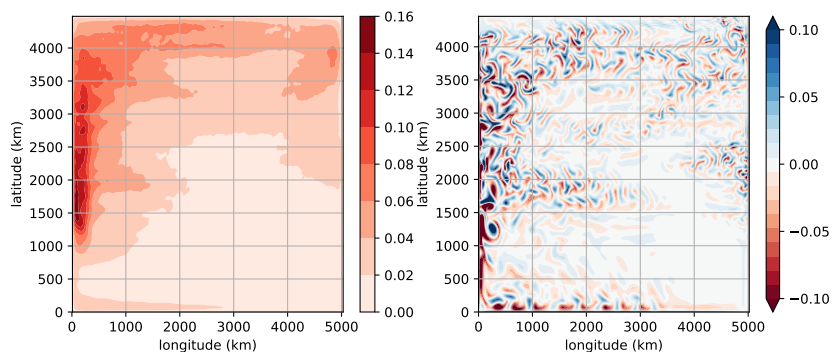
Downloaded from <http://journals.ametsoc.org/jcli/article-pdf/doi/10.1175/JCLI-D-19-0921.1/4961484/jcli190921.pdf> by guest on 02 July 2020



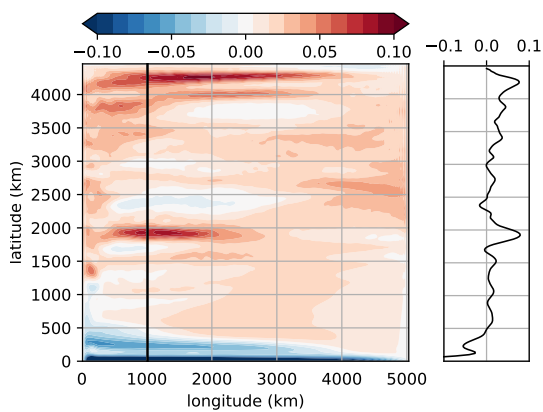
806 FIG. 1. First Complex EOF calculated on 1 year averaged 3D temperature outputs, accounting for 60% of
 807 the variability. Top left: real part of the SST, top right imaginary part of the SST. Middle left: real part of the
 808 meridional section (longitude = 1800km) shown by a red line on the top left and right panels, middle right:
 809 imaginary part of the same section. Black contours show isotherms of the time mean temperature. Bottom: real
 810 (red solid) and imaginary (red dotted) part of the principal component of the first CEOF. The blue line shows the
 811 MOC strength (in Sv) at the latitude ($y_{max} = 3500\text{km}$) and depth ($z_{max} = -500\text{m}$) where the time mean MOC
 812 is maximum.



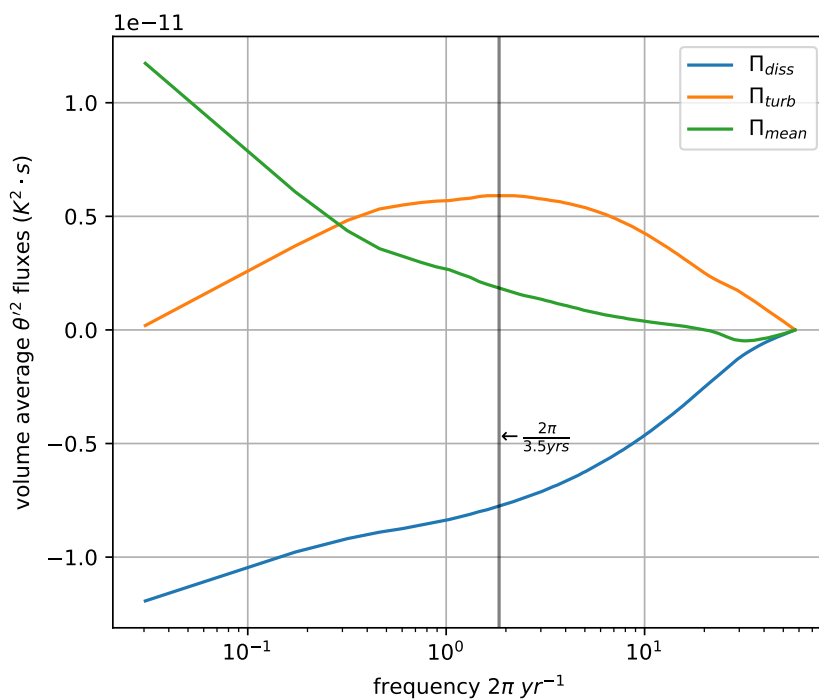
813 FIG. 2. Volume average of the temperature spectrum as a function of frequency calculated from 1 year average
 814 output over 500 years (black line) and 3 days average output over 50 years (dashed black line). The largest peak
 815 and its harmonic respectively have a frequency of $2\pi/42 \text{ yr}^{-1}$ and $2\pi/21 \text{ yr}^{-1}$ (blue vertical lines). The $2\pi/3.5$
 816 yr^{-1} limit between Low and High frequencies (defined in subsection c) is shown with a black vertical line. MOC
 817 frequency spectrum calculated with Welch's method on 1 year average outputs over 500 years is in red.



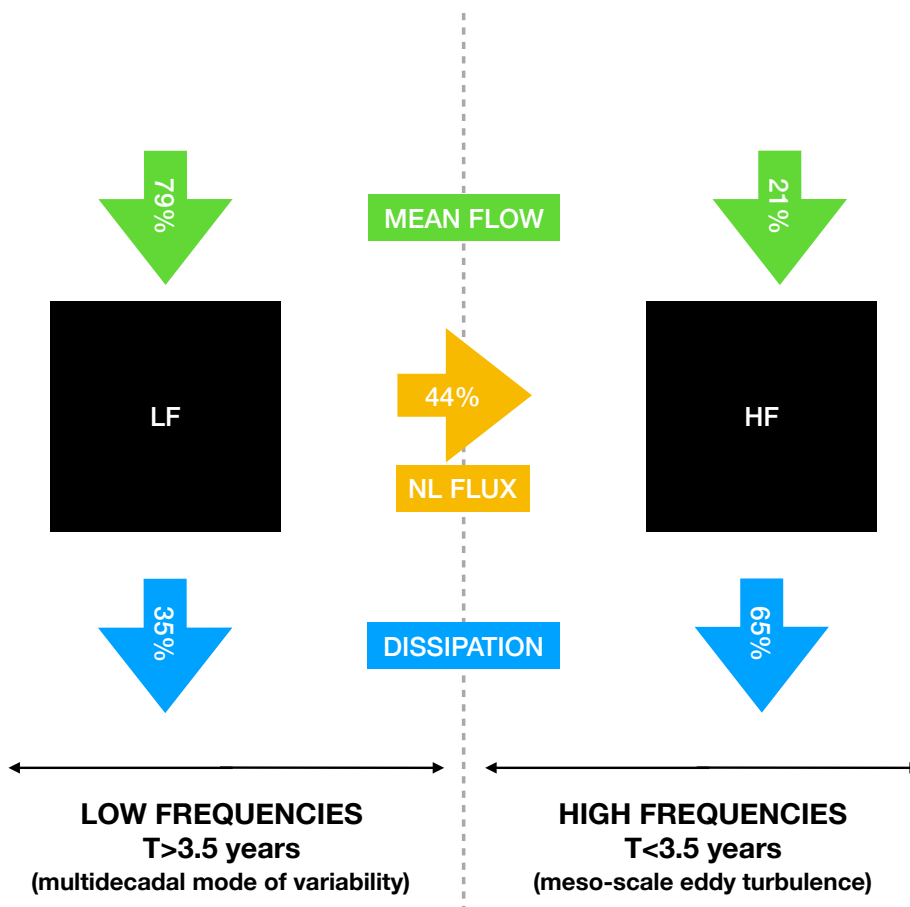
818 FIG. 3. Left: standard deviation of Sea Surface Height (in m) using 3 days output on a 50 year period with 2
819 years running average removed. Right: snapshot of the ratio of the surface relative vorticity $\partial_x v - \partial_y u$ and f .



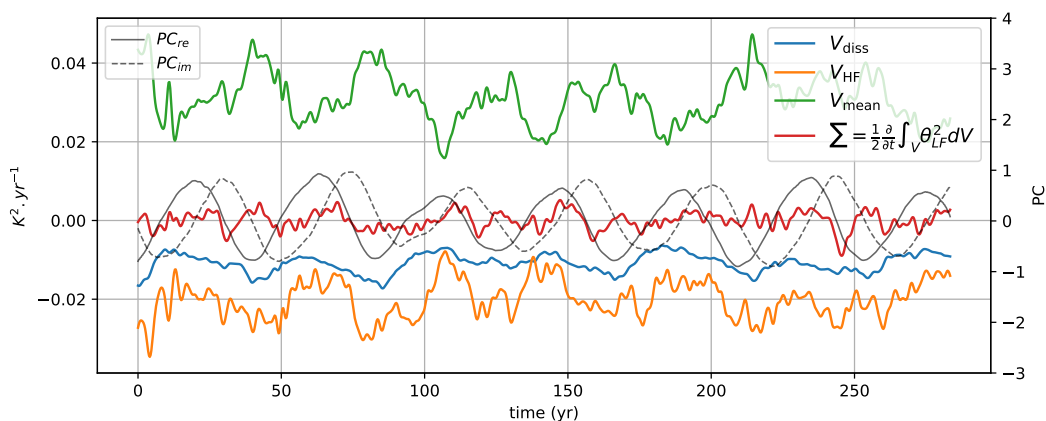
820 FIG. 4. Left: time mean of the surface zonal velocity (ms^{-1}). Right: meridional section of the time mean
821 surface zonal velocity at longitude=1000 km (as shown by the black vertical line on the left panel).



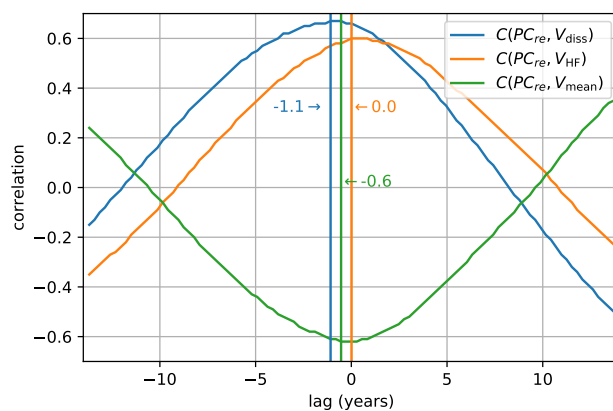
822 FIG. 5. Temperature variance fluxes as a function of frequency for Π_{diss} (blue), Π_{turb} (orange) and Π_{mean}
 823 (green) as defined by Eq. (7), (8), (9) and (10). The vertical line at $2\pi/3.5$ years corresponds to the maximum
 824 of Π_{turb} and is used to separate the High and Low-Frequencies (i.e. eddy turbulence and multidecadal mode of
 825 variability).



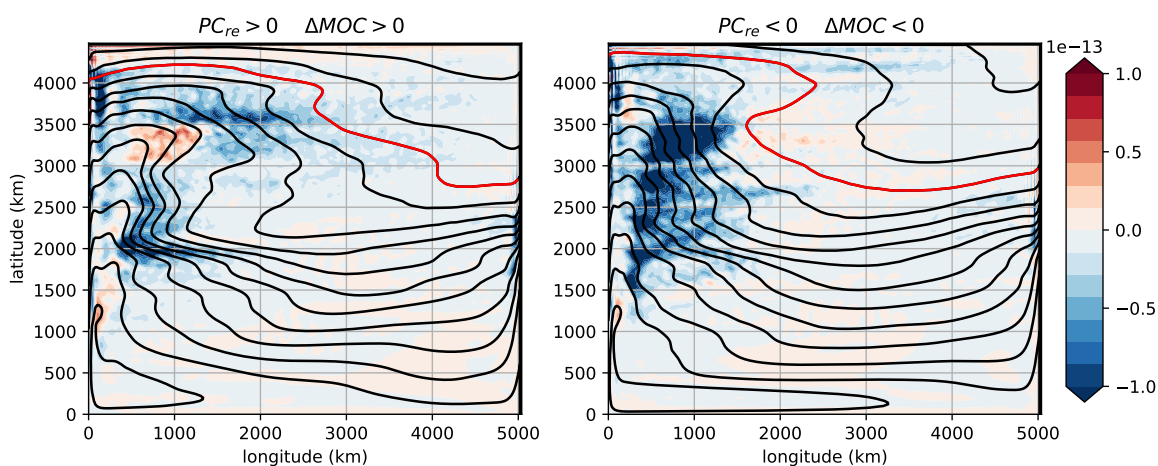
826 FIG. 6. Schematic showing the temperature variance fluxes between low- and high-frequencies reservoirs.
 827 All percentages are expressed with respect to the total flux of temperature variance from the mean flow
 828 ($\Pi_{\text{mean}}(\omega_{\text{min}})$). Direction of arrows shows direction of the fluxes. Π_{diss} is in blue, Π_{mean} is in green and Π_{turb} is
 829 in orange. The sum of all arrows for each reservoir is 0.



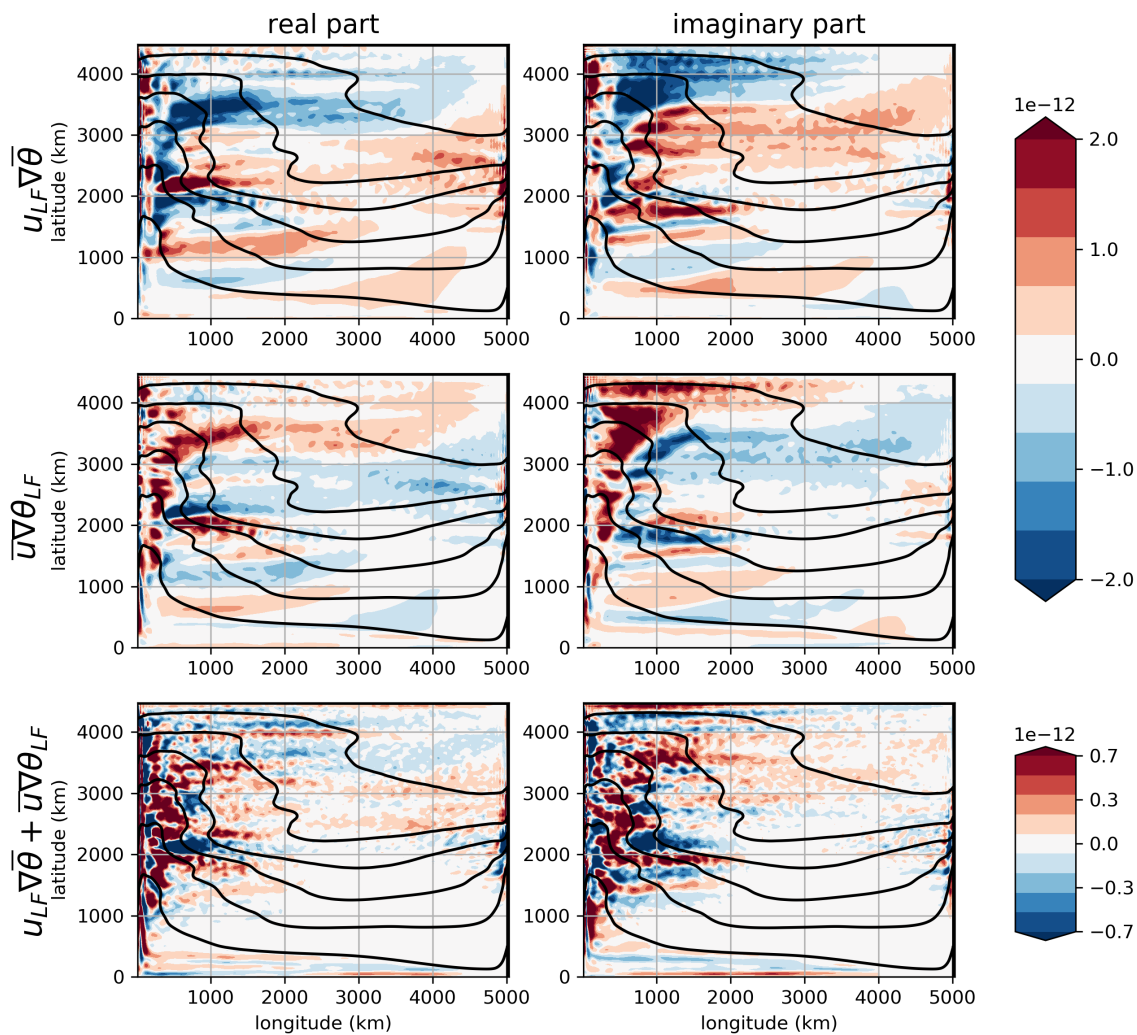
830 FIG. 7. Time evolution of the volume averaged low-frequency temperature variance budget. The effect of
 831 mean temperature gradient V_{mean} is in green, the effect of parameterised diffusion V_{diss} is in blue, the effect of
 832 high-frequencies on low-frequencies V_{HF} is in orange, and the sum of all terms (equal to $\frac{1}{2} \frac{\partial}{\partial t} \int_V \theta_{LF}^2 dV$) is in red.
 833 The real and imaginary part of the leading CEOF PC are shown with respectively solid and dashed black lines.



834 FIG. 8. Lagged correlation between the PC's real part (PC_{re}) and V_{diss} (in blue), V_{HF} (in orange) and V_{mean}
 835 (in green). The lagged times (in years) for the minimum correlation between PC_{re} and V_{diss} and V_{HF} ; and for the
 836 maximum correlation between PC_{re} and V_{mean} are shown with three vertical lines.



837 FIG. 9. Effect of eddies (in $\text{K}^2 \text{s}^{-1}$) on the low-frequency temperature variance. V_{HF}^{int} (see Eq. (27)) is time
 838 averaged on two time periods defined by the sign of the real part of the leading temperature CEOF PC (see Fig.
 839 1). Left panel: $PC_{re} \geq 0$, right panel: $PC_{re} < 0$. The sign of the MOC anomaly (ΔMOC) is shown in each panel
 840 title and is the same as the PC_{re} sign. The superimposed black contours show the temperature averaged on the
 841 same depths and times, in red is the 4.5 K contour. V_{HF}^{int} follows the largest LF temperature gradients that appear
 842 in the western half of the basin.



843 FIG. 10. Contribution of $\mathbf{u}_{LF} \cdot \nabla \bar{\theta}$ (middle panels), $\bar{\mathbf{u}} \cdot \nabla \theta_{LF}$ (top panels) and their sum $\bar{\mathbf{u}} \cdot \nabla \theta_{LF} + \mathbf{u}_{LF} \cdot \nabla \bar{\theta}$
 844 to the low-frequency temperature budget. Each term is regressed respectively against the real part (left panels)
 845 and imaginary part (right panels) of the leading CEOF PC. Note the different colorbar. Units: K s^{-1} . $\mathbf{u}_{LF} \cdot \nabla \bar{\theta}$ is
 846 partly compensated by $\bar{\mathbf{u}} \cdot \nabla \theta_{LF}$ due to the “non-Doppler shift” as explained in section 4 b.